Materials Science & Engineering A 830 (2022) 142223

Contents lists available at ScienceDirect

Materials Science & Engineering A

journal homepage: www.elsevier.com/locate/msea

Creep and creep damage behavior of stainless steel 316L manufactured by laser powder bed fusion

L.A. Ávila Calderón [a,*], B. Rehmer [a], S. Schriever [a], A. Ulbricht [a], L. Agudo Jácome [a], K. Sommer [a], G. Mohr [a,b], B. Skrotzki [a], A. Evans [a]

[a] Bundesanstalt für Materialforschung und –prüfung (BAM), Unter den Eichen 87, 12205, Berlin, Germany
[b] Institute of Machine Tools and Factory Management, Chair of Processes and Technologies for Highly Loaded Welds, Technische Universität Berlin, Straße des 17 Juni 135, 10623, Berlin, Germany

ARTICLE INFO

Keywords:
Creep behavior
Additive manufacturing
LPBF 316L
Micro-computed tomography
Hot tensile properties
Creep damage
Microstructure

ABSTRACT

This study presents a thorough characterization of the creep properties of austenitic stainless steel 316L produced by laser powder bed fusion (LPBF 316L) contributing to the sparse available data to date. Experimental results (mechanical tests, microscopy, X-ray computed tomography) concerning the creep deformation and damage mechanisms are presented and discussed. The tested LPBF material exhibits a low defect population, which allows for the isolation and improved understanding of the effect of other typical aspects of an LPBF microstructure on the creep behavior. As a benchmark to assess the material properties of the LPBF 316L, a conventionally manufactured variant of 316L was also tested. To characterize the creep properties, hot tensile tests and constant force creep tests at 600 °C and 650 °C are performed. The creep stress exponents of the LPBF material are smaller than that of the conventional variant. The primary and secondary creep stages and the times to rupture of the LPBF material are shorter than the hot rolled 316L. Overall the creep damage is more extensive in the LPBF material. The creep damage of the LPBF material is overall mainly intergranular. It is presumably caused and accelerated by both the appearance of precipitates at the grain boundaries and the unfavorable orientation of the grain boundaries. Neither the melt pool boundaries nor entrapped gas pores show a significant influence on the creep damage mechanism.

1. Introduction

Additive manufacturing of metallic materials (metal AM) is an emerging technology that is increasingly the subject of research activities and industrial application. Some general advantages of the technology are the geometrical design freedom, the savings in weight and operational costs, e.g., in tooling and warehouses, and the potential to reduce lead times [1]. Therefore, metal AM is establishing itself gradually as a new group of manufacturing processes of general relevance complementary to casting, forging, or machining. Regarding its use, apart from the successful production of parts in the jewelry, sport, or medical sector, there have also been recent advances in the manufacturing of parts used in safety-relevant applications [1,2]. However, metal AM still faces challenges regarding its use in specific safety-relevant applications that could benefit from its advantages, and that involve, for instance, creep or thermo-mechanical fatigue. The reasons for the delay of this technological breakthrough are the lack of a deeper understanding of process-structure-properties relationships and the limited availability of material properties data [3,4].

The austenitic stainless steels 316L and 316LN, with different nitrogen contents, and commonly grouped as 316L(N), are commonly investigated materials in their AM variants. The conventional variant has several fields of application. 316L is, for instance, used as surgical stainless steel and also to manufacture bolts and nuts with an operating temperature range from −200 °C to 400 °C [5]. Additionally, it is used in nuclear reactors, where the operating temperatures can reach up to 625 °C [6,7]. Additively manufactured 316L has also made some steps to start being applied in safety-relevant applications [8]. However, at least to the authors' knowledge, there are no AM 316L parts being used in applications where creep plays a role. Regarding the state of the research, there are up to date only a few publications dealing with the creep behavior of LPBF 316L [9–12]. More investigations are still needed to gain a full understanding. Li et al. [9] reported creep tests at temperatures of 550 °C, 600 °C and 650 °C. They tested LBPF 316L as

* Corresponding author.
E-mail address: luis.avila@bam.de (L.A. Ávila Calderón).

https://doi.org/10.1016/j.msea.2021.142223
Received 23 July 2021; Received in revised form 19 October 2021; Accepted 19 October 2021
Available online 27 October 2021

well as wrought 316H steels. Williams et al. [12] tested double notched test pieces at 650 °C. Yoon et al. [11] tested small test pieces (3 mm diameter, 22.5 mm gauge length) at 650 °C. Jong et al. [10] performed small punch creep tests at 650 °C. Conventionally manufactured 316L (N) on the other hand has been intensively studied regarding the creep behavior, see e.g. [13–17]. Sasikala et al. [14], for instance, investigated 316 and 316LN steels and their weldments at 600 °C and 650 °C and performed extensive metallographic investigations to rationalize the observed properties.

Overall, the microstructure of AM metals is highly dependent on process conditions, and the scanning and deposition strategy [18,19]. The process conditions prevailing during the LPBF process generate unique microstructural features in the manufactured alloys, and each manufacturing strategy delivers in principle a different microstructure. In the resulting unique microstructures, the different typical AM features are present in varying degrees and length scales and thus may influence in different respects the mechanical properties, including the creep properties [20]. This variability of the AM microstructure makes it challenging to investigate mechanical properties such as creep that depend on many factors. Some microstructural features considered relevant to creep behavior are briefly presented below.

One of the most relevant process conditions that affects the microstructure is the high cooling rate. In LPBF, they can be around 10^5 K/s to 10^6 K/s compared to 10^0 K/s to 10^2 K/s which is the typical range for casting processes [4]. The high cooling rates often lead to high residual stresses and as-built anisotropic and metastable microstructures [4]. In LPBF 316L and other AM metals, the high cooling rates contribute to forming a solidification cellular structure (referred to hereafter as cellular structure) with high dislocation density (10^{14} m^{-2} for LPBF 316L in [21]) accumulated along the cell walls and subgrain boundaries that have different dislocation densities [22–25]. Furthermore, in LPBF 316L, this cellular structure has a localized concentration of elements such as Cr and Mo and segregation of nano precipitates along the cell walls [25,26]. The nano precipitates were identified for LPBF 316L in [25] as transition-metal-rich silicates. The effect of the cellular structure on certain material properties of 316L has been reported in literature. At room temperature during tensile deformation, its presence contributes substantially to creating a steady work-hardening ability, large uniform tensile elongations, and high yield strengths, due to, i.e., the resulting high dislocation density [25–28]. The effect on the creep behavior has been noted but so far not investigated thoroughly. Li et al. [9] suggested that the cellular structure has an effect on the stress dependency of the creep rate and pointed out that it limits the capacity of dislocation multiplication, which leads to achieving the minimum creep rate rapidly.

Apart from high residual stresses, as-built anisotropic and metastable microstructures, columnar grains, and the cellular structure, AM microstructures include gas porosity, lack of fusion voids, melt pool boundaries, and often textured microstructures with unique grain morphologies. These material characteristics and manufacturing flaws may as well influence the creep behavior [9,11,12], especially in terms of the damage accumulation. Yoon et al. [11] showed occurrence of cracking at grain boundaries. Williams et al. [12] reported large transgranular cracks and intergranular creep micro-cracks that apparently mainly extended from lack of fusion defects and to a lesser extent from gas porosity. The intergranular micro-cracks were suggested to be a product of the coalescence of creep cavities at the grain boundaries and were seen at grain boundaries perpendicular as well as nearly parallel to the building direction. The final fracture was due to the branching and linking of the micro-cracks through several defects and across multiple layers. The rupture was ultimately transgranular in nature. The investigated material had a defect volume fraction smaller than 0.5%. In the work of Li et al. [9], grain boundary cracking was the dominant failure mode. The grains were highly elongated, and the cracks grow primarily along the grain boundaries perpendicular to the loading direction. A few large cracks mixed with a high density of microcracks dispersed at grain boundaries were seen. The defect volume fraction in the analyzed region was 0.10%, being higher and more concentrated towards its center (0.18%).

Furthermore, the chemical composition, the stacking fault energy (SFE), and the precipitation kinetics may also influence the creep behavior of 316L(N) stainless steel as reported for the conventional variant [14,17,29]. Sasikala et al. [14] reported in their study the precipitation of $M_{23}C_6$-type carbides and intermetallic σ-phase. The precipitation kinetics was dependent, i.e., on the initial chemical composition, e.g., the nitrogen and carbon content, and phases, e.g., the amount of delta ferrite.

This study aims to contribute to the understanding of the creep behavior of LPBF 316L through the presentation and discussion of experimental results related to creep deformation and damage behavior. Data on the material properties and results that represent a first step in understanding the creep deformation and damage mechanisms are presented. As a benchmark to assess the material properties, a conventionally manufactured variant of the same alloy is tested. The results are compared to existing literature data. Within the study, the LPBF 316L and the conventional 316L, are subjected to hot tensile tests and constant force creep tests at 600 °C and 650 °C. The creep behavior of both materials is characterized in terms of characteristic values (e.g., rupture times, creep strain, minimum creep strain rate). The influence of the microstructure is discussed. Because of the complex hierarchical nature of AM microstructures, the microstructure and the creep damage behavior of the LPBF material are characterized by different destructive and non-destructive techniques across different length scales and compared to the behavior of the conventional variant.

2. Materials and methods

2.1. Conventional and LPBF material and specimens

The LPBF specimens are produced on a commercial LPBF machine of type SLM 280 HL (SLM Solutions Group AG, Lübeck, Germany) under argon gas atmosphere, using stainless steel 316L powder with a particle size distribution between 10 μm and 45 μm. Detailed information about the LPBF system and the 316L powder feedstock are described in a previous publication [30]. The specimens used for this investigation are rectangular prisms of the dimensions 13 mm × 20 mm × 112 mm manufactured vertically on the build plate. Rectangular prisms are manufactured instead of near-net shape specimens to avoid variations of properties due to geometrical changes in the building direction, which might influence the resulting microstructure [35]. The z-axis dimension is 114.5 mm to compensate for cutting waste during part removal from the baseplate. The specimens are manufactured using a meander stripe scanning strategy with a rotation of the scanning direction by 90° after every layer. The scan vectors proceeded parallel to the edges of the specimen and are not interrupted within the cross-sections. The following process parameters are applied: laser power of 275 W, scanning velocity of 700 mm/s, hatch distance of 0.12 mm, layer thickness of 0.05 mm, substrate preheating of 100 °C and inter layer time of approx. 65 s. Further details can be found in [30,35]. All specimens are heat-treated at 450 °C for 4 h under argon gas atmosphere while still attached to the base plate. The cooling takes place in the furnace in the gas atmosphere. The heat treatment aims to partially relieve the residual stresses while avoiding substantial changes in the microstructure.

A hot-rolled sheet of austenitic stainless steel 316L (1.4404/X2CrNiMo17-2-2) according to DIN EN 10028-7 [36] is used as conventional material. The sheet is 20 mm × 1000 mm x 500 mm (Outokumpu PSC Germany GmbH, Heidenheim, Germany). After hot rolling, the material is solution annealed at 1100 °C and subsequently quenched in water. The manufacturer obtained the sheet from a larger plate by plasma cutting. The sheet is mechanically cut into single blocks with dimensions 135 mm × 20 mm x 20 mm to obtain test pieces. 20 mm were left unused from all sides of the sheet to avoid possible edge effects.

All blocks are oriented longitudinally in the rolling direction. The blocks aimed for the manufacturing of the tensile and creep test pieces are selected from random locations within the sheet.

The tensile and creep test pieces are machined from the middle region of the conventional blocks and the LPBF rectangular prisms. Therefore, the centers of gravity from the test pieces coincide with the centers of gravity of the conventional blocks and the LPBF rectangular prisms. Table 1 shows the actual composition of the two investigated 316L variants as determined for this study. The composition of both materials is determined on one piece of each material. Mn, Cr, Mo and Ni are determined with X-ray fluorescence spectroscopy, C and S are determined with combustion analysis; N is determined with carrier gas hot extraction. Si and P are determined with inductively coupled plasma atomic emission spectroscopy (ICP-AES). The values in Table 1 confirm that both investigated variants are 316L (and not 316LN) according to DIN EN 10028-7 [36]. Throughout this article, the additively manufactured material is referred to as LPBF material and the conventionally manufactured as HR material.

2.2. Microstructure characterization, evaluation of damage and microstructural changes after failure

The microstructure of the LPBF 316L specimens investigated in this study has been partly characterized by Charmi et al. in [30]. A comprehensive texture analysis with electron backscatter diffraction (EBSD) was reported in that study, and the internal porosity of the tensile test piece geometry was described with μCT. The microstructure features a 110 crystallographic texture and a checkerboard grain morphology in a view perpendicular to the building direction [30]. The morphology is the result of the layer wise 90° rotation of the scan vectors [30]. In [30], the initial porosity of a tensile test piece made from the same batch of AM specimens investigated in this study was characterized. The segmented pores in all the test pieces were spherical and were assumed to be gas pores. The measured porosity was much smaller than 0.01%, and the pores were evenly distributed along the volume.

In the present study, a further characterization of the initial microstructure using optical microscopy (OM), μCT and transmission electron microscopy (TEM) is performed. To characterize the porosity, two creep test pieces are measured by μCT. To characterize the failure behavior and to gain an insight of the creep damage mechanism of both materials, cross-sections of selected tested test pieces, one conventional and one LPBF, test piece are metallographically analyzed after fracture. Metallographic investigations using optical, scanning electron microscopy with EBSD, energy dispersive X-ray spectroscopy (SEM-EDS), and non-destructive investigations with μCT are performed.

For OM, the analyzed pieces, initial and postmortem investigations, are first cold mounted and subsequently ground down to the plane of analysis with 180 P SiC abrasive paper. After that, they are further ground in three steps using SiC abrasive papers of 320 P, 600 P and 1200 P grain size. Finally, they are mechanically polished using polishing cloths MD Dac, MD Nap, and MD-Chem (Cloeren Technology GmbH, Wegberg, Germany). The grain sizes are 3 μm, 1 μm and 0.2 μm, the polishing suspensions DiaPro Dac, DiaPro Nap-B (Struers GmbH, Willich, Germany) and Mastermet II (Buehler, ITW Test & Measurement GmbH, Esslingen, Germany), and the polishing agents Diamond (2x) and SiO respectively. For grinding and polishing, a semi-automatic Buehler Phoenix 4000 machine (Buehler, ITW Test & Measurement GmbH, Esslingen, Germany) is used. For optical microscopy and SEM, the mounted samples are additionally etched for about 3 s – 5 s using Bloech & Wedl etchant (30 ml dest. H_2O, 30 ml HCl conc. 37% and 0.6 gr $K_2S_2O_5$).

The OM images are taken with an inverted metallurgical microscope GX71 (Olympus Europa SE & CO. KG, Hamburg, Germany). EBSD measurements and SEM-EDS analysis are done on a scanning electron microscope (SEM) Leo Gemini 1530 VP (Carl Zeiss Microscopy GmbH, Germany) equipped with a high-resolution EBSD detector e$^-$Flash^{HD} and an EDS detector -XFlash 5030 (Bruker Corporation, United States). The software package ESPRIT 1.9.4 (Bruker Corporation, United States) was used for acquisition, indexing and post-processing of the EBSD and the EDS data. For EBSD analysis, the voltage is 20 kV, the minimum and maximum pixel sizes used are 0.94 μm and 6.32 μm, the beam current is 10 nA and the pattern size 160 × 120 pixels. For EDS Analysis, the pixel size is 24 nm. Furthermore, a Tescan VEGA3 (Tescan Orsay Holding, a. s. Brno, Czech Republic) scanning electron microscope is used for selected analysis.

Scanning transmission electron microscopy (STEM) is used to make a comparative qualitative characterization of the dislocation density at room temperature of both investigated materials. To perform this investigation, two samples were prepared, one from the HR and one from the LPBF material in the heat-treated initial state. The samples came from the material close to the middle of the HR blocks and of the LPBF rectangular prisms. To this end, 0.5 mm thin slices were extracted in the case of the LPBF material parallel to the building direction and in the case of the HR material perpendicular to the rolling direction. The building direction in the LPBF material and the rolling direction in the HR material are equivalent to the loading direction of the creep test pieces. These slices are subsequently ground on both sides to a quality of 1200 P emery paper to reach a thickness of about 100 μm. These disks are then electrolytically thinned to electron transparency in a twin-jet Tenupol-3 device (Struers GmbH, Denmark) at 24 °C and 25 V with a flow rate of 3.1 a. u. with a mixture of 95% acetic acid and 5% hydrochloric acid. TEM was conducted at an acceleration voltage of 200 kV in a JED-2200FS (JEOL Ltd., Japan) microscope equipped with a field emission gun, an in-column "omega"-type energy filter and a scanning (S)TEM device.

The μCT data is acquired on the commercial μCT scanner GE v|tome|x 180/300 (GE Sensing & Inspection Technologies GmbH, Germany) using the 300 kV X-ray source at a voltage of 200 kV, a current of 50 μA. A silver prefilter of 0.25 mm thickness is used. A voxel size of $(10\ \mu m)^3$ is achieved. The data is filtered using the plug-in *non local means denoising* [37,38] in the open source software Fiji [39]. To analyze the reconstructed volumes, the commercial software VG Studio MAX Version 3.3 (Volume Graphics GmbH, Germany) was used in combination with the open source software iLastik [40].

2.3. Creep and tensile testing

2.3.1. Tensile testing

Tensile tests on 8 mechanical test pieces were conducted to obtain strength and deformation values that enable the interpretation of the results of the creep tests. For each material, three tests at 600 °C and one at 650 °C according to DIN EN ISO 6892-2 [41] were performed. The characteristic deformation values: percentage elongation after fracture (A) and the reduction of area (Z) are calculated based on measurements on the test pieces before and after the tests.

A 100-kN Instron testing machine (Model: 4505, class 1 calibration, Instron GmbH, Darmstadt, Germany) equipped with a split tube furnace (Model: 3210, ATS Applied Test Systems Inc.) was used. To measure the

Table 1
Chemical composition in wt %.

	Fe	C	Si	Mn	P	S	Cr	Ni	Mo	N
LPBF	Balance	0.013	0.53	0.97	0.007	0.0044	17.70	12.70	2.33	0.077
Hot rolled	Balance	0.017	0.46	1.28	0.030	0.0044	16.90	10.10	2.03	0.045

strain, an MTS water-cooled high-temperature extensometer (Model: 632.51C-05, at least class 1, nominal gauge length 21 mm) is applied. Tensile test pieces B 6 × 36 according to DIN 50125 [42] with cylindrical cross-section, ground ($R_z \leq 3.2$), with threaded ends M10, total length 60 mm, diameter of parallel length 6 mm, and length of reduced parallel section 36 mm are used.

All tensile tests are carried out strain-rate-controlled up to approximately 20% engineering strain. If possible, the extensometer is removed after that, and the test is further driven in crosshead-speed control. The strain rate for the tests is 7×10^{-5} 1/s, the crosshead speed 0.00252 mm/s (0.1512 mm/min). These values correspond to the suggested range in method A of the standard [41]. The heating ramp to the test temperature lasts about 3 h, and the test pieces are soaked for around 70 min at the respective testing temperature before starting the tests. The loading direction coincides with the building direction in the LPBF material and with the rolling direction in the HR material.

2.3.2. Creep testing

Twelve creep tests at constant force are performed until rupture of the test pieces according to DIN EN ISO 204:2019–04 [43]. The tests are conducted on both LPBF and HR 316L at 600 °C and 650 °C using initial stress levels ranging from 175 MPa to 275 MPa with a 25 MPa increment. Three BAM-modified 20-kN creep testing machines (Mohr & Federhaff AG, Mannheim, Germany) are used. All three machines feature calibration class 1 of the applied force according to DIN EN ISO 7500-2 [44] and are equipped with three-zone furnaces (custom-made by Heraeus Holding GmbH, Hanau, Germany). The initial loading force (full weight) that delivers the initial stress level was applied shock-free by hand. The loading time ranged from 15 s to about 90 s, and the loading speed from 3.05 MPa/s to 11.67 MPa/s. A pre-force of 1 kg was applied before heating the test pieces to keep the extensometer fixed during the initial heating.

Calibrated temperature data acquisition units SCXI-1102 from National Instruments are used (National instruments Kft., Debrecen, Hungary). The temperature control takes place via the temperature signal from the furnaces. The temperature of the test pieces is measured using three thermocouples type S tied along the gauge length. The thermocouples are calibrated based on EURAMET/cg-08 [45], and the temperature measurement chain is calibrated based on EURAMET/cg-11 [46]. MTS water-cooled high-temperature single-side extensometers (Model: 632.51C-03, class 1, nominal gauge lengths 50 mm and 52 mm) are used to measure the strain.

The data acquisition takes place initially, before initial loading, every 5 s. During the initial loading, the data acquisition time interval is set to 0.1 s. After initial loading, it is set to 1 min up to max. 10 min, depending on the test duration.

Proportional test pieces with cylindrical cross-section, ground ($R_z \leq 3.2$), with threaded ends M12, total length of 100 mm, diameter of in the gauge length of 8 mm, and 60 mm length of reduced parallel section are used. The percentage elongation after fracture (A) is not measured at the test pieces. The reduction of area after rupture (Z_u) is determined according to the standard [43].

The stress levels used for each material and temperature are stepwise determined based on the partial results. The objective was to have at least two coincident stress levels for both types of materials at each tested temperature. The choice of the testing temperatures is based on the service temperature of the alloy (see section 1) and on available literature data. Similar to the hot tensile test procedure, the heating ramp lasts approximately 2.5 h (~4 °C/min), and the test pieces are soaked for approximately 1.5 h at testing temperature before performing the tests. As in the case of the tensile tests, the loading direction coincides with the building direction in the LPBF material and with the rolling direction in the HR material.

3. Results

3.1. Microstructure

Fig. 1 shows representative images of the microstructure of the two material conditions. Fig. 1a and b are optical micrographs from the etched LPBF material, and Fig. 1c and d from the HR material. The z direction corresponds to the loading direction in both cases (building direction in the case of the LPBF material and rolling direction in the case of the HR material).

Fig. 1a is a micrograph taken from a plane perpendicular to building direction of the LPBF material. The checkerboard grain morphology described by Charmi et al. [30] is visible. Fig. 1b is a micrograph from a plane parallel to the building direction. There, the grains have an irregular shape which is a product of the epitaxial grain growth of remelted zones. They are stacked on top of each other in parallel columnar regions and show the “ripple-like” shapes as described elsewhere [25]. In both figures, the grain boundaries (GB) and the melt pool boundaries (MPB) are identified (black arrows). Apart from the light micrographs shown in Fig. 1, a 4 mm × 3 mm EBSD scan is analyzed regarding phases and grain size description. The microstructure is fully austenitic, as the light micrograph in Fig. 1b suggests by the lack of any other visible phases following etching. The mean grain size, determined in a plane parallel to the building direction, is 75 μm. It is calculated as the mean diameter value of equivalent circles with the same area of each grain. The underlying misorientation (MO) angle is 15°. The μCT analysis of the porosity in the two investigated test pieces reveals that all segmented pores are spherical. Therefore, they are assumed to be gas pores. The porosity is much lower than 0.01%, and the pores distribute evenly along the volume. Since the porosity results of the investigated creep test pieces coincide with the results reported in [30], one can conclude that this porosity is typical for this material.

Concerning the HR material, Fig. 1c shows a micrograph from a plane perpendicular to rolling direction and Fig. 1d from a plane parallel to the rolling direction, z corresponds to the rolling direction and x and y to the transverse and normal (through-thickness) direction. The grain morphology is equiaxial, and twins are present, accounting for a considerable proportion of the grains. On both micrographs, delta ferrite can be identified. The delta ferrite was identified using phase analysis in three EBSD scans. It appears in different sizes and has mostly an elongated morphology, which depending on the analyzed plane can also appear circular or oval. As suggested by Fig. 1c and d, the microstructure is primarily austenitic with ca. 0.9% delta ferrite, as determined from two EBSD scans. The grain size is determined in a plane perpendicular to the rolling direction in the band contrast (BD) image of an EBSD measurement using the planimetric procedure according to ASTM E112-13 [48], and it corresponds to grain size number, G, of 7.0, which corresponds to ca. 30 μm equivalent average diameter. This variant of 316L is well suited as a benchmark because it represents an idealized fine, fully recrystallized, equiaxed microstructure, which is suitable for multiple applications.

In terms of the dislocation substructure, Fig. 2 shows representative bright field (BF) STEM images of the initial microstructure at room temperature of the investigated materials: on the top, Fig. 2a and d show the coordinate systems of the sample and of the crystal for the regions investigated, Fig. 2b and e show low-magnification micrographs, where white regions mark the higher magnified images shown in Fig. 2c and f. The LPBF material is presented on the left of Fig. 2 (a, b and c), while HR material is on the right (d, e and f). In the LPBF material, x and y are parallel to the tower walls, as also indicated in Fig. 1a and b. In the HR material, y is the normal (plate through-thickness) direction, and x the transverse direction, as presented in Fig. 1c and d.

The LPBF material has a high dislocation density as qualitatively shown. In Fig. 2b, three subgrains, with widths below ≈10 μm, have been partially captured on the left, center and right, as can be recognized by the overall different contrasts of these regions. The subgrain

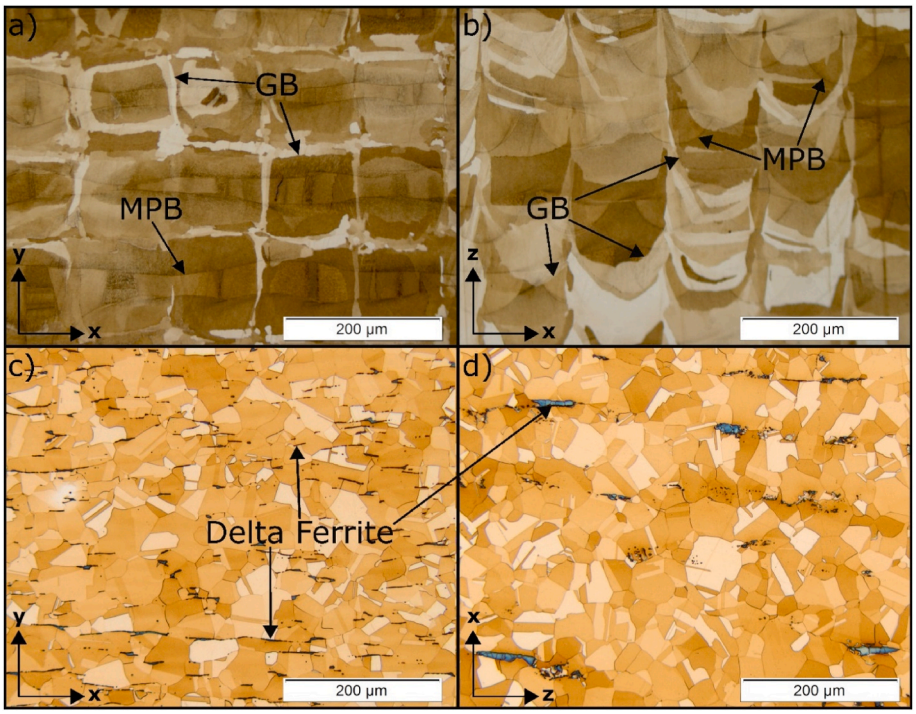

Fig. 1. Initial microstructures (OM) at room temperature after etching. a) and b) LPBF material, z corresponds to the building direction c) and d) HR material, z corresponds to the rolling direction.

boundaries (SGB) are exemplarily shown in Fig. 2b and c (black arrows). All these subgrains present similar shapes of cellular structure, with a cell size of roughly 0.5 µm–1 µm. At this scale, the microstructure of the LPBF material is clearly characterized by dislocation networks that decorate mostly the walls of cellular structures, as becomes apparent in the magnified image of Fig. 2c. Furthermore, localized concentration of Cr and Mo and segregated nano precipitates also decorate the cell walls (not shown in Fig. 2). The dislocations also spread into the cell cores. All dislocations seem to be perfect dislocations without apparent signs of dissociation. The arrangement of the dislocations is clearly different in the subgrain boundaries than in the cell walls: in the subgrain boundaries, dislocation walls are narrower, whereas the cell walls are wider, and the dislocations are tangled. This finding coincides with previous descriptions of the microstructure of LPBF 316L at this scale, e.g., in [21]. Altogether, the LPBF material has a hierarchically organized microstructure consisting of the grains seen in Fig. 1, and the subgrains with cellular structures within them. Before heat treatment, the dislocation substructure looks identical at all scales studied (results not shown).

In the images corresponding to the HR material, Fig. 2e and f, the round-shaped darker region is delta-ferrite, and was identified in the TEM by an increase in Cr and Mo via EDS, as well as by selected area diffraction patterns (SADP) on this particle and on several similar particles. The inset SADP in Fig. 2f was acquired on the round appearing particle at a sample tilt ≈11° away from the tilt in the BF STEM image. In this material, other than these delta ferrite particles, twins (see Fig. 1c and d) represent large planar defects with serrated interfaces, at which dislocations interact. The overall dislocation density is at least an order of magnitude lower than for the LPBF material, and they have larger mean free paths between interfacial obstacles, e.g., delta/gamma interfaces, or twin and large-angle boundaries. A common observation throughout the HR material is that the dislocation density, while overall low, increases towards these planar defects, e.g., close to the delta-ferrite particle in Fig. 2e. From trace analysis of Fig. 2e, it is clear that the few present dislocations are localized on rows along just a few slip planes, i.e., shear bands (see schematic lattice planes and directions in Fig. 2d). A closer look into the region squared in white on Fig. 2e reveals that many of these dislocations are dissociated into partials, which reveal the darker contrasts spanning between dislocation pairs on slip planes that are not edge-on, see black arrows in Fig. 2f.

3.2. Tensile and creep testing

3.2.1. Tensile tests

The characteristic values determined from the test pieces are listed in Table 2, and, where possible, the mean values and standard deviations. The LPBF material features at both test temperatures a significantly higher yield strength (about 2.5x higher in the LPBF than in the HR material). The increase in ultimate tensile strength is almost negligible (5%–7.5%). The ductility is lower but still close to the values of the HR material (30%–50% lower elongation to fracture in the LPBF material). Characteristic values at room temperature for the LPBF material are reported in [30].

3.2.2. Creep tests

3.2.2.1. On-load response. The total strain during the creep tests, e_t, eq. (1), consists of the time-independent initial loading strain component, e_{ti}, and the time-dependent creep strain component, e_f. The initial loading strain component, e_{ti}, is the strain reached by the end of the application of the load and the creep strain, e_f, is the strain developed by the material under constant load with time. The initial loading strain, e_{ti}, in turn has an elastic and a plastic component, e_e and e_i, respectively, eq. (2).

$$e_t = e_{ti} + e_f \tag{1}$$

$$e_{ti} = e_e + e_i \tag{2}$$

Fig. 3a and Fig. 3b show the strain response to the initial loading (e_{ti}, e_e and e_i). Fig. 3a shows the initial strains, e_{ti}, that each material reaches at each combination of applied stress and temperature. The LPBF material (black symbols) features much smaller initial strains, e_{ti}, (<0.3%) than the HR material (>3%) at all test conditions. Furthermore, e_{ti} does

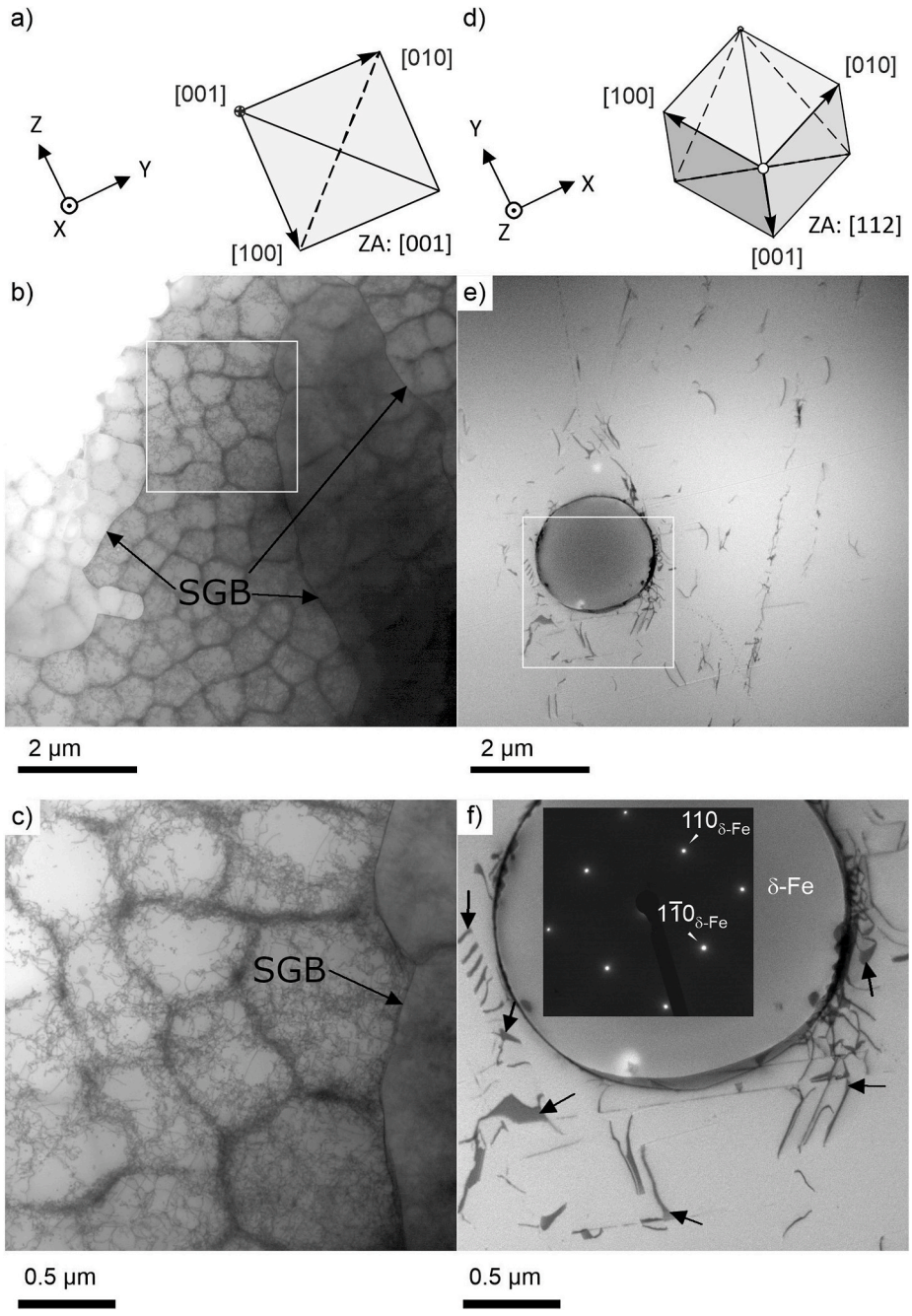

Fig. 2. BF STEM images from the initial microstructures at room temperature. a), b) and c): LPBF material; c), d) and f): HR material. b) and e): low magnification. c) and f) higher magnification (see white boxes). In the coordinate systems shown in a) and d), z corresponds to the building direction in the LPBF material, images a) to c), and to the rolling direction in the HR material, images d) to f).

Table 2
Results of hot tensile tests: yield strength, $R_{p0.2}$, ultimate tensile strength, $R_{m,}$ elongation at fracture, *A* and reduction of area, *Z*. Calculated mean values and standard deviation (SD) when possible.

		LPBF						HR					
T	°C	600					650	600					650
Test piece no.	–	1	2	3	Mean	SD	1	1	2	3	Mean	SD	1
$R_{p0.2}$	MPa	315	323	316	318	4	282	120	128	117	122	6	118
R_m		372	381	385	379	7	328	360	365	362	362	3	305
A	%	43	43	37	41	3	21	–	63	56	60	5	42
Z		52	53	50	52	2	32	–	81	84	83	2	82

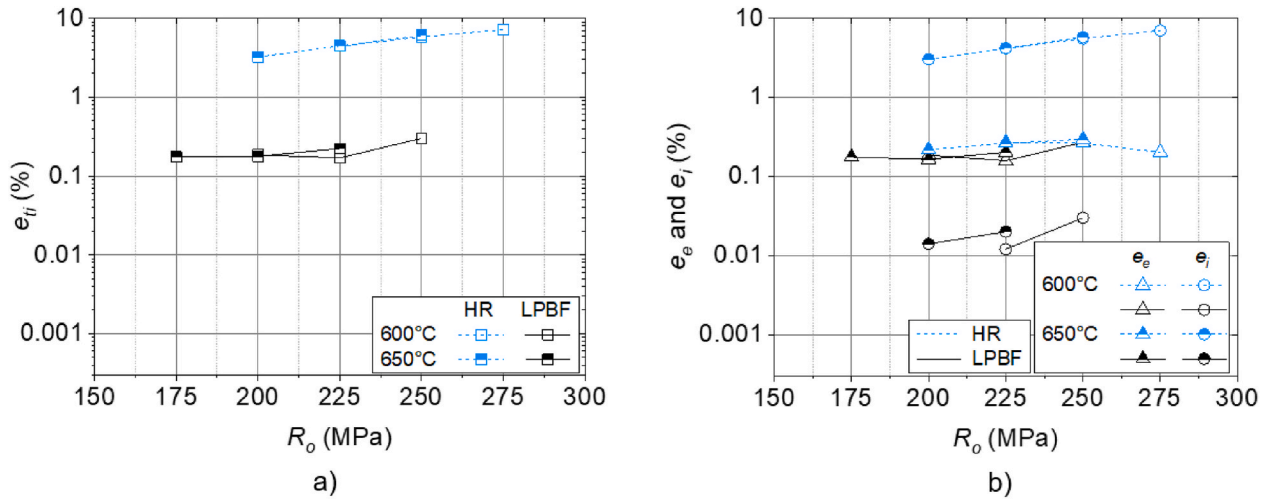

Fig. 3. a) Total strain on application of force, b) elastic and plastic components. Note that the lines connecting the data points do not represent a fit.

not change significantly with the variation of the temperature for the two materials.

Fig. 3b provides additional information on the elastic and plastic components, e_e and e_i, respectively, of the initial loading strain, e_{ti}. The initial strain of the LPBF material consists mainly of the elastic component, e_e, (triangular symbols) whereas the HR material deforms mainly plastically (circular symbols represent e_i). Note that the y axis is plotted at a logarithmic scale to visualize the changes. The plastic components of the LPBF material are equal to zero at 650 °C/175 MPa and at 600 °C/200 MPa.

3.2.2.2. Creep response. Fig. 4 shows the results regarding the creep response. Three different curves are shown: a creep strain, e_f, vs. time, t, graph, Fig. 4a; a creep rate, $\dot{e}_f$, vs. t graph, Fig. 4b, and a creep rate vs. total strain graph, Fig. 4c. The creep strain e_f vs. t graph, Fig. 4a, is obtained from the raw strain data plotted against the time. Due to a failure data acquisition, there is a gap in the data at 650 °C/200 MPa at approximately 150 h. To determine the $\dot{e}_f$ vs. t graph, Fig. 4b, smoothed strain data using a rolling average is differentiated with respect to time. Subsequently, the obtained creep rate data is again smoothed with a rolling average. To obtain the $\dot{e}_f$ vs. e_t graph, Fig. 4c, the smoothed creep rate data is plotted against the original unsmoothed strain data.

3.2.2.2.1. Time to rupture. Commonly, the creep behavior is plotted in terms of creep strain over time, Fig. 4a. A comparison of the individual curves shows that the LPBF material (black symbols) has shorter times to rupture, t_u, than the conventional material (blue symbols) at the same test parameters. Fig. 5 shows the creep rupture diagram represented as applied stress, R_o, vs. rupture time, t_u, for the two materials at the two tested temperatures. The times to rupture, t_u, of the LPBF material (black symbols) for the two tested temperatures and at all applied stresses are shorter than those from the HR material (blue symbols, dashed lines). The creep lifetimes are fitted with a power function of the form $f(x) = a{\cdot}x^b$, to show that the straight line-fit for the two materials approximates the tendency with increasing stress at both temperatures.

3.2.2.2.2. Creep ductility. A value that, alternatively to the elongation after fracture, A_u, serves to describe the creep ductility indirectly is the total plastic deformation at failure (e_p in equation (3)). Making a description based on e_p is only reasonable if all test pieces break either inside or outside of the extensometer gauge length, which is the case in this study, where all test pieces broke at similar positions relative to the grips outside the extensometer gauge length. e_p, can be derived from the results shown in Figs. 3b and 4. Fig. 4 shows that, in addition to the fact that the LPBF material has smaller plastic initial loading strains, e_i, (see Fig. 3b), it has smaller creep strains, e_f, compared to the HR material at all test conditions. The LPBF material has lower creep ductility than the HR material at all combination of test parameters.

$$e_p = e_t - e_e = e_i + e_f \tag{3}$$

3.2.2.2.3. Time in creep stages. From a microstructural point of view, a representation of the creep strain rate, $\dot{e}_f$, as a function of time, Fig. 4b, or strain is more insightful, since the creep strain rate directly represents the material's response to loading [49]. In addition to the observations from Fig. 4a and b shows that the LPBF material reaches the minimum creep strain rate at the same stress level and temperature faster, i.e., has a shorter primary creep stage, than the HR material. Furthermore, Fig. 4b shows that the LPBF material has a shorter secondary creep stage, and a more accelerated damage behavior, i.e., shorter tertiary creep stage, than the HR material. Fig. 6 shows the durations of the primary, t_1, secondary, t_2, and tertiary creep stages, t_3, and represents in a clearer manner the findings regarding Fig. 4b. The plot also shows that the differences between durations of the creep stages at the same stress level and temperature are significant (note that the y axis is plotted on a logarithmic scale). For all durations of creep stages in Fig. 6, the difference between LPBF (black symbols) and HR material (blue symbols, dashed lines) appears to become smaller with increasing applied stress, as in the case of the times to rupture in Fig. 5. To show that, the data points are fitted with a power function. For both materials the duration of the tertiary creep stage is about one order of magnitude higher than of the other two stages. The times from the onset of the secondary and tertiary creep stages, t_{12} and t_{23}, respectively (eq. (4)) are determined as the limits of a line-fitting performed on the raw data strain vs. time, which is done to determine the minimum creep rate, $\dot{e}_s$. The secondary creep duration, t_2, is determined as indicated in eq. (4) and the duration of the tertiary creep is determined as shown in eq. (5)., whereby t_u represents the time to rupture.

$$t_2 = t_{23} - t_{12} \tag{4}$$

$$t_3 = t_u - t_{23} \tag{5}$$

3.2.2.2.4. Creep strain at minimum creep rate. A diagram of the creep strain rate, $\dot{e}_f$, over the total strain, e_t, until failure, Fig. 4c, helps to further understand the differences in the materials behavior. On the one hand, it shows again (see Fig. 3a) that the initial loading strain, e_{ti}, is smaller in the LPBF material than the HR material for all tested combinations of parameters. To enlighten this point, note that the x-axis represents the total strain, e_t, and not the creep strain, e_f, or the total plastic strain, e_p. Therefore, the initial strain, e_{ti}, is visible as an offset in e_t (before creep starts, $\dot{e}_f$ is inexistent). This offset is most evident for the conventional material. On the other hand, Fig. 4c suggests that the LPBF

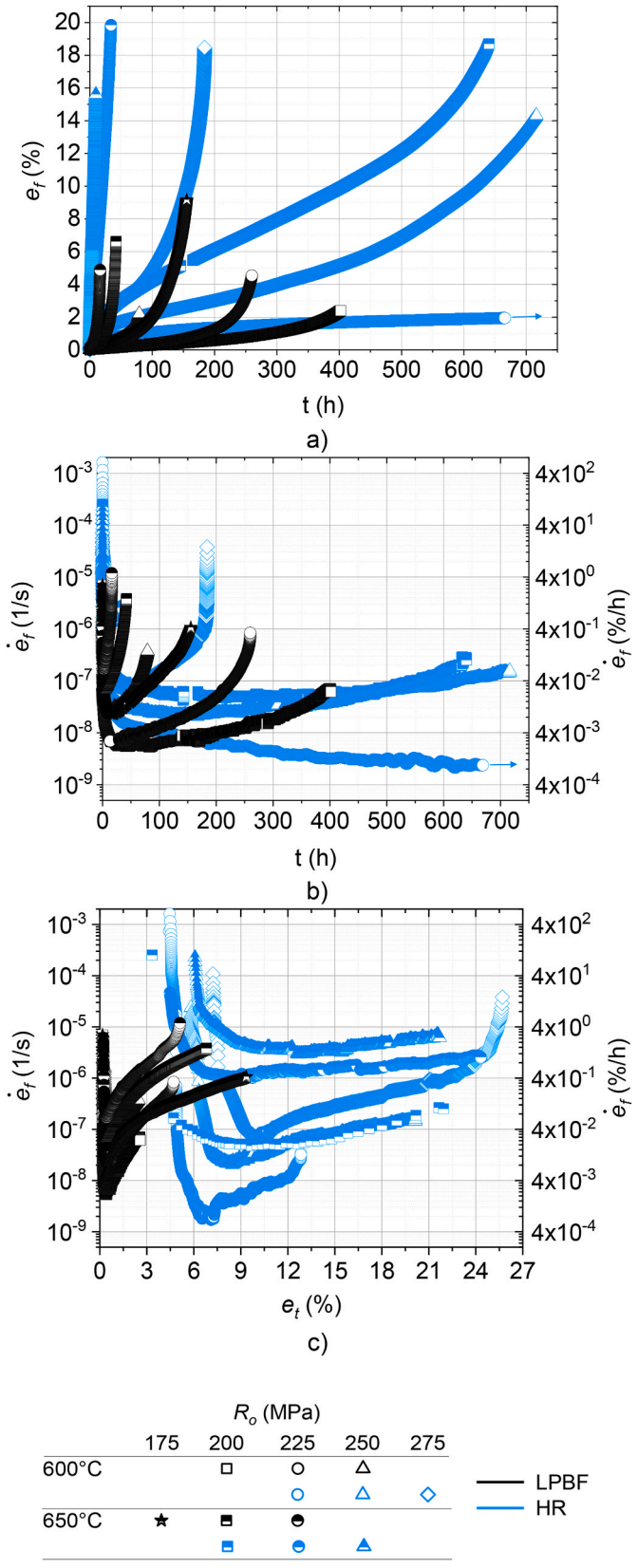

Fig. 4. a) Creep strain vs. time, b) creep strain rate vs. time, and c) creep strain rate vs. total strain.

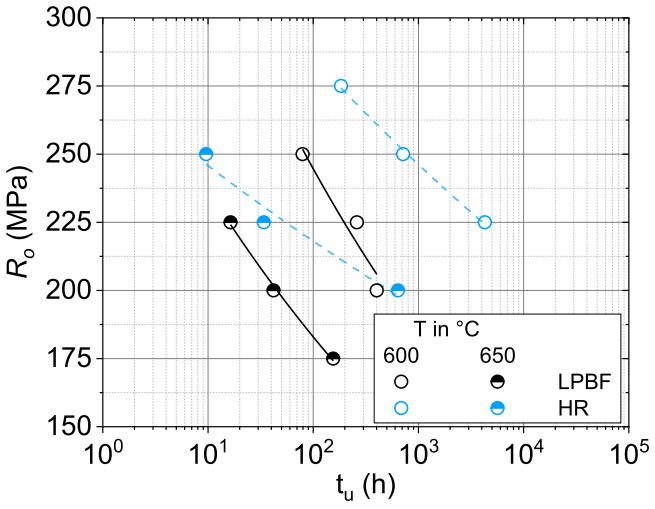

Fig. 5. Applied stress vs. time to rupture.

material reaches the minimum creep rate at smaller total strains, e_t, compared to the HR material at the tested temperatures and stress levels. The same is, of course, valid for the creep strain, e_f. To further analyze this latter point, Fig. 7 shows the creep strain corresponding to the minimum creep rate at each applied stress, e_f at $\dot{e}_s$, which is determined as the creep strain value corresponding to the time of the onset on secondary creep stage, t_{12}, (eq. (4)). The figure confirms that the LPBF material (black symbols) reaches the minimum creep rate at significantly lower strains (<0.2%), around one order of magnitude lower, compared to the HR material (blue symbols, dashed lines; >2%). Furthermore, the stress dependency of e_f at $\dot{e}_s$, of both materials at each test temperature is negligible. The minimum creep rate, $\dot{e}_s$, is read from Fig. 4a by performing a linear interpolation between the data points. The values obtained for $\dot{e}_s$ are presented in Table 3. The dependence of $\dot{e}_s$ on stress and temperature is discussed in section 4, subsection 4.2.3.

Table 3 shows an overview of the studied parameters and results of the creep tests. Relevant characteristic values are shown. A comparison of the values obtained for the elongation at fracture from the tensile tests (Table 2) with the creep strain in the creep tests (Table 3) shows that the decrease in material ductility is much higher (up to 3x) for the LPBF material in the creep tests compared to the tensile tests at same tested temperatures than for the HR variant.

3.3. Evaluation of creep damage and microstructural changes after failure

This section summarizes the results of the postmortem investigations of two selected creep test pieces, one LPBF and one HR, both tested at T = 600 °C and R_o = 225 MPa. The results shown in this section represent a first insight on the creep damage mechanisms operating, with focus on the LPBF material. These test pieces were selected because they have the largest difference in rupture times of all matching pairs of test pieces (4027 h). Besides, 600 °C represents a more application-relevant temperature compared to 650 °C.

3.3.1. HR material

Fig. 8 depicts the creep fracture characteristics of the HR creep test piece. Fig. 8a is a μCT reconstruction of the analyzed creep test piece. The shape of the test piece visible in this image (light gray) is representative for all tested test pieces of the HR material. They all show a pronounced necking that indicates ductile fracture, and which is also evident in the values of reduction of area, Z_u, in Table 3. Fig. 8b is a detailed view from a cut section at the fracture region; some damage in the form of voids can be recognized (blue arrows). Away from the fracture the microstructure is much less deformed than at the fracture

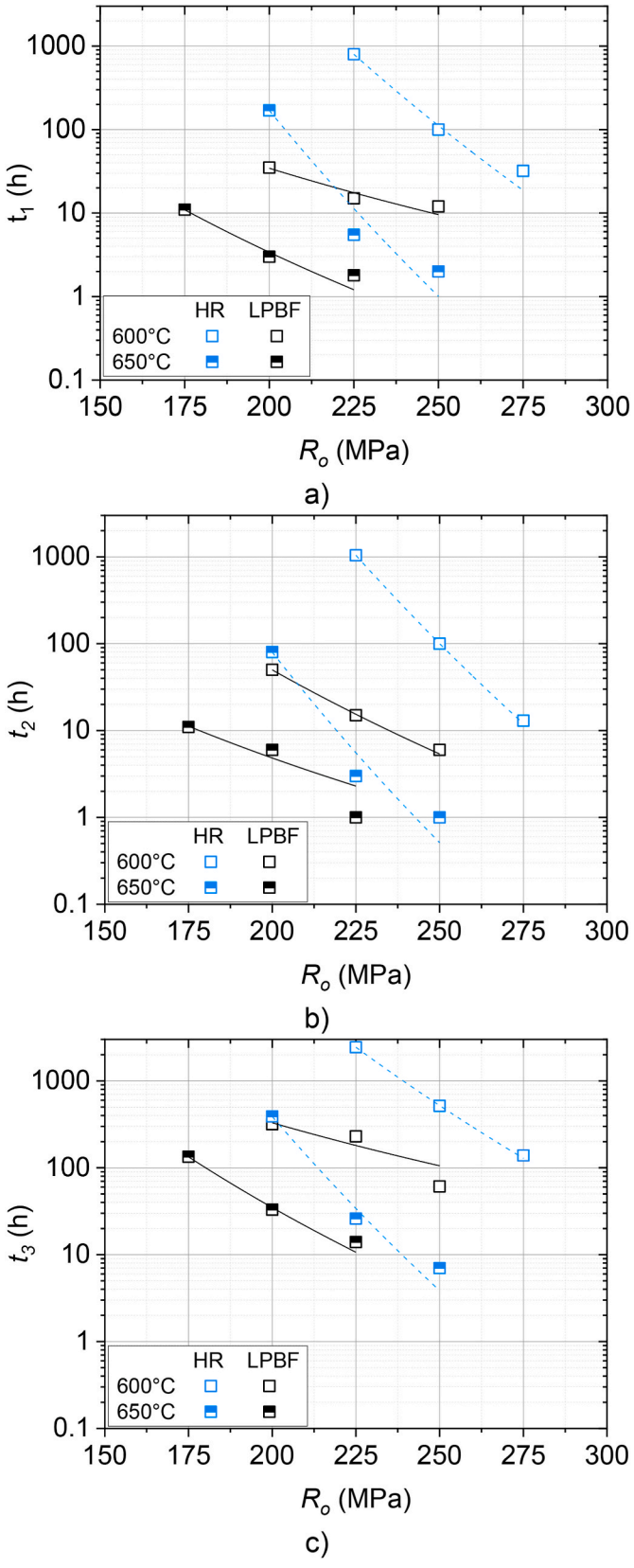

Fig. 6. a) Time spent in primary, b) secondary and c) tertiary creep stages, vs. applied initial stress.

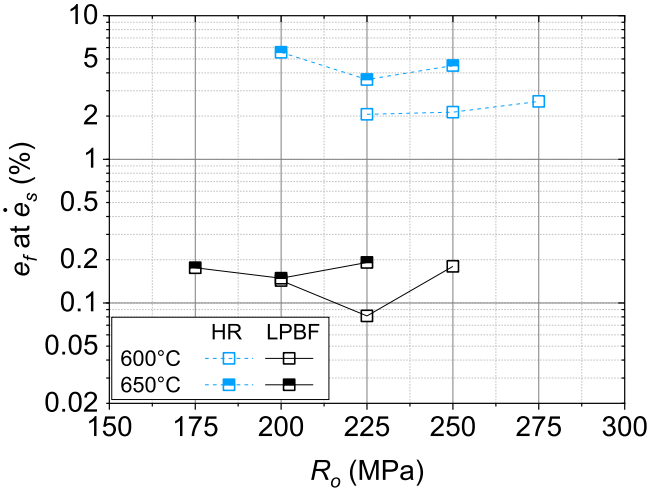

Fig. 7. Creep strain at minimum creep rate vs. applied initial stress.

region (see Fig. 8c). The larger deformation in the necked region is visible in the larger aspect ratio of the grains. In regions further away from the fracture area (not shown here) the grains are less deformed than grains shown in Fig. 8c, and are optically similar to the initial morphology shown in Fig. 2. All combined, Fig. 8 reveal that the creep deformation accumulates the most near the fracture surface in the necked region. The μCT reconstruction, Fig. 8a, reveals furthermore that the voids' population is sparse and localized in the fracture region with a tendency towards the middle region of the test piece. The voids are visible mostly as blue features. In Fig. 8b, only a few round-to-oval voids are observed. The final fracture is transgranular in nature. Additionally, Fig. 8b and c suggest that either the initially present delta ferrite or a transformed product is present after the test.

3.3.2. *LPBF material*

The postmortem characterization of the LPBF creep test piece was first done in terms of internal damage. Fig. 9 shows two- and three-dimensional images obtained with OM and μCT. Fig. 9a shows an OM image of the fracture region of the analyzed creep test piece. The test piece shown is representative for all tested LPBF creep test pieces, which exhibit almost no necking. The brittle fracture behavior can also be derived from the low reduction of area (Z_u) as shown in Table 3. Fig. 9b shows a μCT reconstruction of the analyzed creep test piece. The shorter and the larger ends of the test piece were separately scanned and then joined virtually. A large number of cavities (mostly blue) are present. The cavities' irregular shape corresponds, at first sight, the shape of the grain and the melt pool boundaries. Their size lies in the order of the grain size reported in subsection 3.1. Besides, these types of cavities were not found in the initial state of the test pieces. Therefore, they are assumed to be associated to creep damage and are called microcracks from now on. The later analysis with OM on the etched sample, Fig. 11, reveals that they originate at the grain boundaries, i. e intergranular. The microcracks are ordered in columns parallel to the build direction. The microcracks do not only concentrate in the immediate region of close to the fracture. In the longer part of the fractures test piece they can be found throughout the whole captured gauge length. In the shorter part they diminish before the end of the gauge length, presumably due to a geometrically conditioned lower local stress. Interconnected microcracks are found close to the fracture surface.

The microcracks identified with μCT have a total volume fraction of 2.65% in the inspected gauge length. The volume fraction includes microcracks and all other cavities that can be present, e.g., gas pores. The scale on the left side of Fig. 9b allows for the differentiation of the cavities depending on their total volume. Bigger microcracks are located

Table 3
Results of creep-rupture tests.

		LPBF						HR					
T	°C	600			650			600			650		
Test piece no.	–	1	2	3	1	2	3	1	2	3	1	2	3
R_o	MPa	200	225	250	175	200	225	225	250	275	200	225	250
t_u	h	402	260	79.3	155	42	16.4	4287	716	184	640	33.9	9.6
$\dot{e}_s$	x 10^{-8} 1/s	0.58	0.7	2.5	2.4	7.6	19	0.21	2.2	7.1	5.0	100	360
e_{ti}	%	0.19	0.17	0.3	0.18	0.18	0.22	4.4	5.8	7.2	3.3	4.5	6.1
e_f		2.4	4.6	2.2	9.2	6.6	4.9	8.4	14.3	18.5	18.7	19.9	15.6
Z_u		7.9	6.5	11	13	10	12	74	75	71	76	74	73

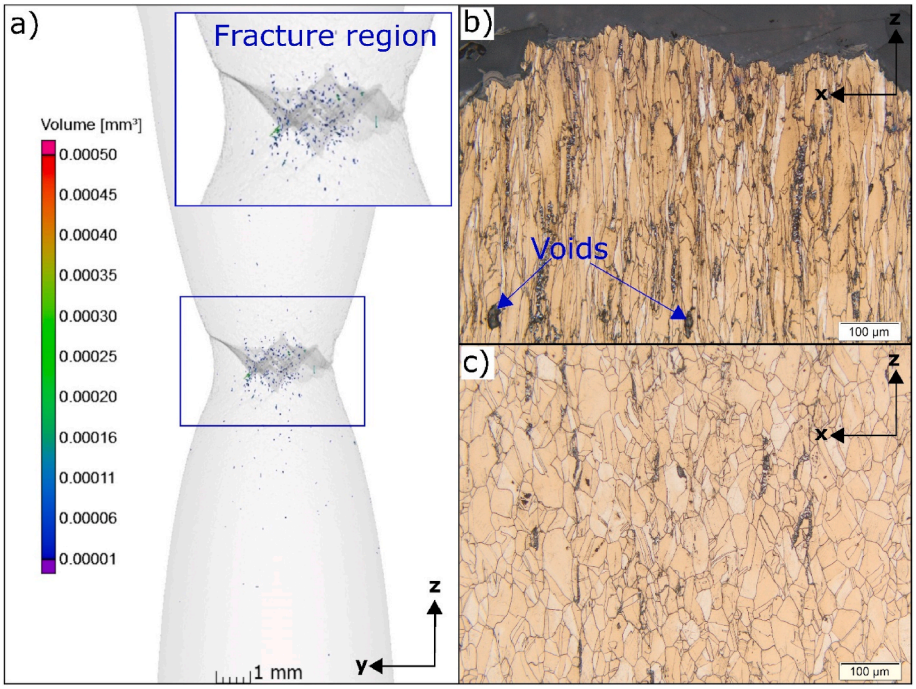

Fig. 8. Conventional material after failure. Test parameters are 600 °C and 225 MPa, z-coordinate corresponds to the rolling and loading direction. a) µCT reconstruction of the analyzed creep test piece. b) and c) representative detail views regions of the fracture region b) and away from it c).

near the fracture surface. These bigger microcracks are either single microcracks or interconnected microcracks (mostly in green). A representative detail from these two types of microcracks is shown on the bottom right of Fig. 9b. The interconnection of microcracks occurs rather rarely.

Fig. 9c shows an OM overview of the fracture surface and an OM detail section (see the black arrow and the corresponding black box). On the fracture surface, the checkerboard pattern presented in Fig. 1 can be recognized. The topography of the fracture surface is not completely flat, which can be seen in Fig. 9a and c. Besides, Fig. 9c schematically shows the plane of the cut section that is subsequently analyzed (blue lines and text), which is slightly tilted from the y-direction. The detailed image elucidates how the section plane cuts through the columns of grains and through the intercolumnar regions (see white text).

Fig. 9d shows OM images of the cut section in an unetched state. The image reveals the existence of a periodically present stripe pattern. This pattern consists of damaged and undamaged regions (see blue text and arrows). In agreement with the results from µCT shown in Fig. 9b, the microcracks are ordered in columns and not only concentrated in the immediate fracture region. Besides, as in Fig. 9b, one can also roughly identify that they are tendentially bigger and more often interconnected near to the fracture surface (see enlarged detail in the bottom of Fig. 9d).

Fig. 9e shows a two-dimensional virtual cut generated from the µCT scan of the larger rest of the test piece that is intentionally created to reproduce the metallographic section of the OM sample preparation (Fig. 9d). To recreate the stripe pattern seen with OM, the virtual cut must be performed not perfectly parallel to the columns of microcracks. From the results of this virtual section, it can be deduced that the material within these striped areas appear to be free of damage and that these areas are located between the microcracks.

In the lower parts of Fig. 9d and e, the fracture region is shown with higher magnification with OM and µCT, respectively. In these two-dimensional images, the microcracks show an inclined double wedge shape. The sharpness of the magnified µCT image is limited by the voxel size of $(10\ \mu m)^3$. The results in Fig. 9 demonstrate that µCT as a 3D non-destructive testing method complements the information delivered by destructive characterization techniques, and enables the analysis of the 3D shape of the damage. Through the freedom of generating arbitrary virtual cuts, it furthermore proves to be a complementary technique that helps to understand the occurrence of the damage.

To further analyze the damage mechanism of the investigated test piece, representative secondary electron (SE) SEM images from the

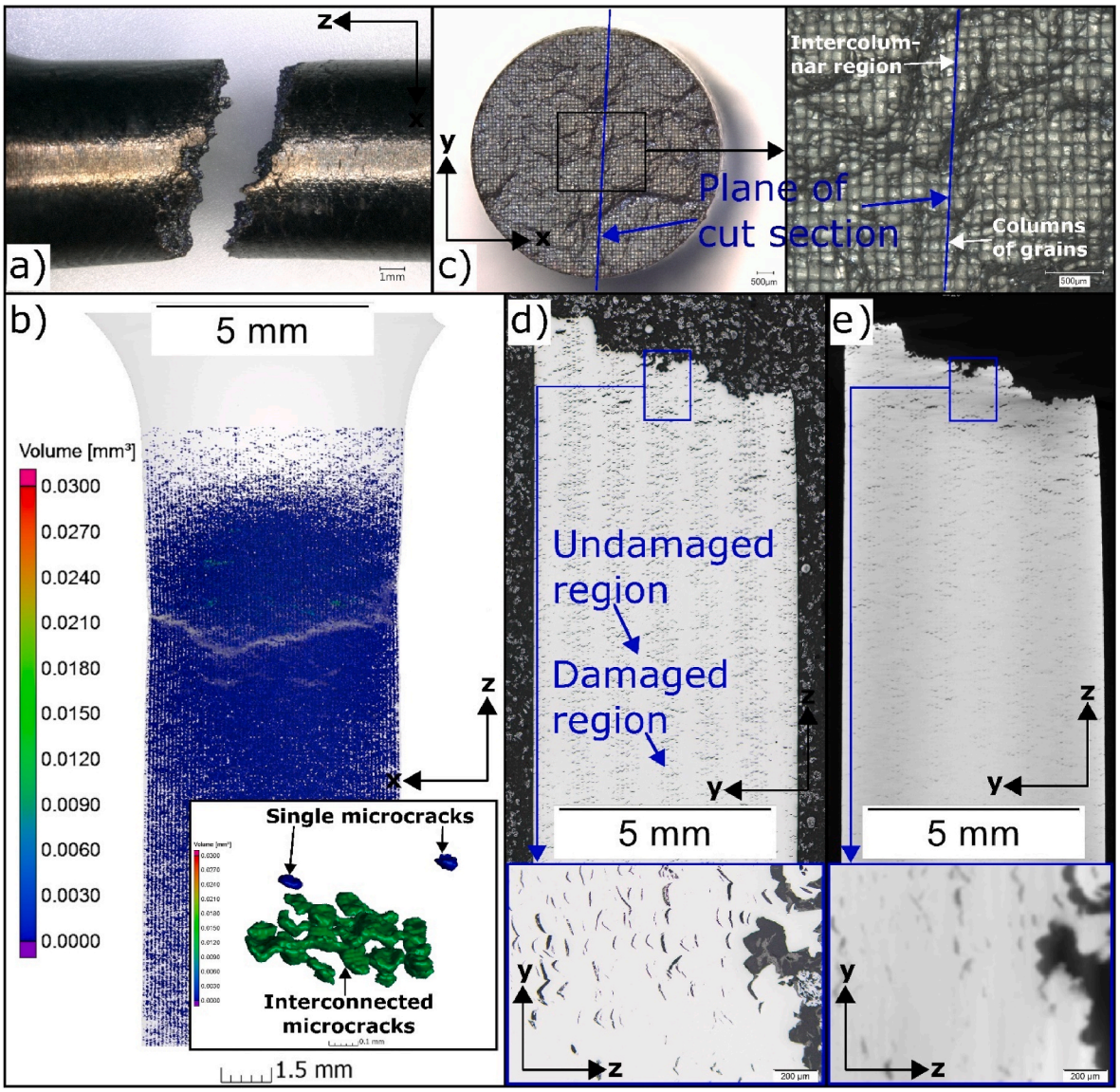

Fig. 9. Creep failure of LPBF test piece at 600 °C and 225 MPa. Visualization of microcracks with destructive (OM) and non-destructive (µCT) characterization techniques. In all images, the z-coordinate corresponds to the building and loading direction. a) Macroscopic view of fracture region and b) µCT scan of the analyzed test piece. c) OM images of the fracture surface, the plane used for the cut section analyzed is schematically shown. d) OM images of the cut section in unetched state, overview (top) and detail (bottom). e) Two-dimensional µCT images of the same cut section (virtual cut), overview (top) and detail (bottom).

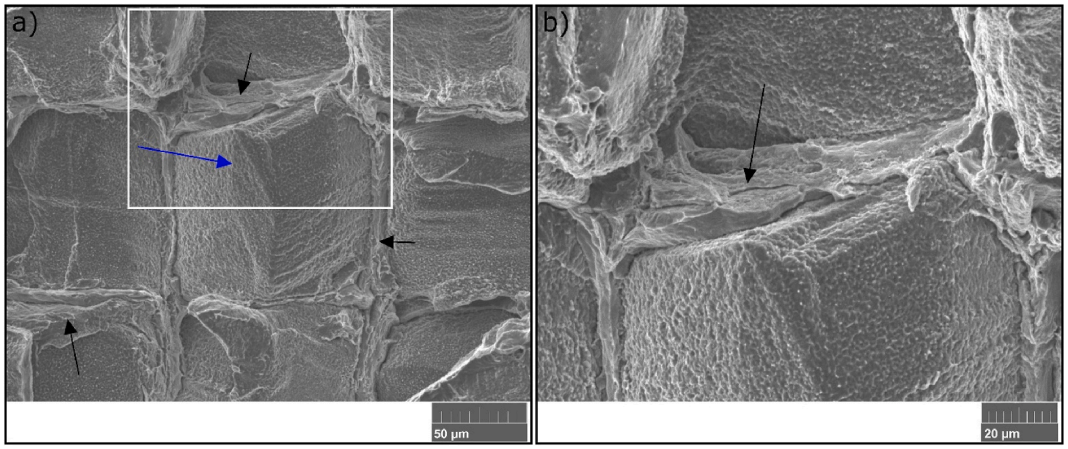

Fig. 10. SE SEM images showing details of fracture surface from LPBF investigated test piece shown in Fig. 9 at a) lower and b) higher magnification. Fracture appears to be overall intergranular with more ductile areas in intercolumnar regions (black arrows).

fracture surface (partly shown in Fig. 9c), are shown in Fig. 10. Fig. 10b is a detailed image from a selected region (white box) of Fig. 10a. In the images, the checkerboard pattern can again be clearly recognized. In the figure, regions with a rather ductile and a rather brittle fracture morphology can be seen. The regions where the failure seems to be more ductile (black arrows) coincide with the intercolumnar regions seen in Fig. 9c (white text). The regions where the failure appears to be more brittle (blue arrows) coincide with the columns of grains, also seen in Fig. 9c (white text). The intercolumnar regions feature a rather ductile-like fracture. The zones that feature brittle-like fracture are located towards the middle of the columns of grains. In these more brittle zones suggesting intergranular fracture, very small dimples are visible, which can be interpreted as ductility on the microscale. The final fracture overall is mainly intergranular.

Complementing the results shown in Figs. 9 and 10, optical micrographs from the cut section after etching are shown in Fig. 11. Fig. 11a represents an overview. Fig. 11b to e are micrographs showing details from regions away and near the fracture surface. Fig. 11b–e show that the microcracks identified in Fig. 9 are located at grain boundaries, i.e., product of intergranular damage (ID, black arrows), and that their propensity is lower in regions away from the fracture surface (Fig. 11b and d). Besides, images shown in Fig. 11b–e demonstrate that microcracks are not forming at melt pool boundaries (MPB, black arrows linked to dashed black lines highlighting them partially). Furthermore, in Fig. 11b–e, round voids can be observed that do not appear to influence cracking. These round voids are assumed to be original gas pores generated by the manufacturing process. In Fig. 11e two of the microcracks are connected (see black circle). These interconnected microcracks are rather seldom as presented in Fig. 9.

Finally, in Fig. 11b and c, one can identify regions with less intergranular damage (ID). These regions are either intercolumnar or within the columns of grains. Within the columns of grains, the regions with less ID correspond to groups of grains that are still connected and do not exhibit open cavities at the grain boundaries. The intercolumnar regions with less damage are visible between the columns of grains where the grain morphology is more elongated in the building (horizontal) direction. In addition, they are visible as stripes with less damage in Fig. 9 or as areas with a different grain morphology in Fig. 11, as shown with dashed boxes in Fig. 11b and c. The presence of these microstructural features as previous mentioned arises because the section is not perfectly parallel to scan direction. Therefore, the section cuts the microstructure at an acute angle, leading to the intercolumnar regions to be clearly visible on the cross-section.

To better understand the mechanisms causing the intergranular damage, the cut section is analyzed in the polished state with SEM-EDS. The analysis of a microcrack tip in the LPBF sample is shown in Fig. 12. In Fig. 12a, results from back-scatter electrons (BSE) measurements show the location of the analyzed microcrack tip within the cut section in overview and in detail (follow blue boxes and arrows). Fig. 12b shows the element EDS maps for four selected elements.

The element maps reveal that there is a depletion of Cr and Mo at the crack tip (black regions) and that Cr- and Mo- rich precipitates form on the submicron-scale (white arrows), close to the resolution limit of this technique. These precipitates are moreover depleted in Fe- and Ni content (black regions in the corresponding element maps). They form at the grain boundaries, where the microcracks appear. The precipitates were also observed through SEM-EDS in the crept conventional material. However, they were generally larger than in the LPBF material and occurred less frequently and also within the grains. Additionally, a small void is visible in the rightmost image of Fig. 12a along the grain boundary. Its size lies below the resolution limit of the µCT scans performed. Such voids are also present near to tips of other microcracks as well as at other grain boundaries in the crept test piece. These small voids are rather rarely observed along the grain boundaries in the

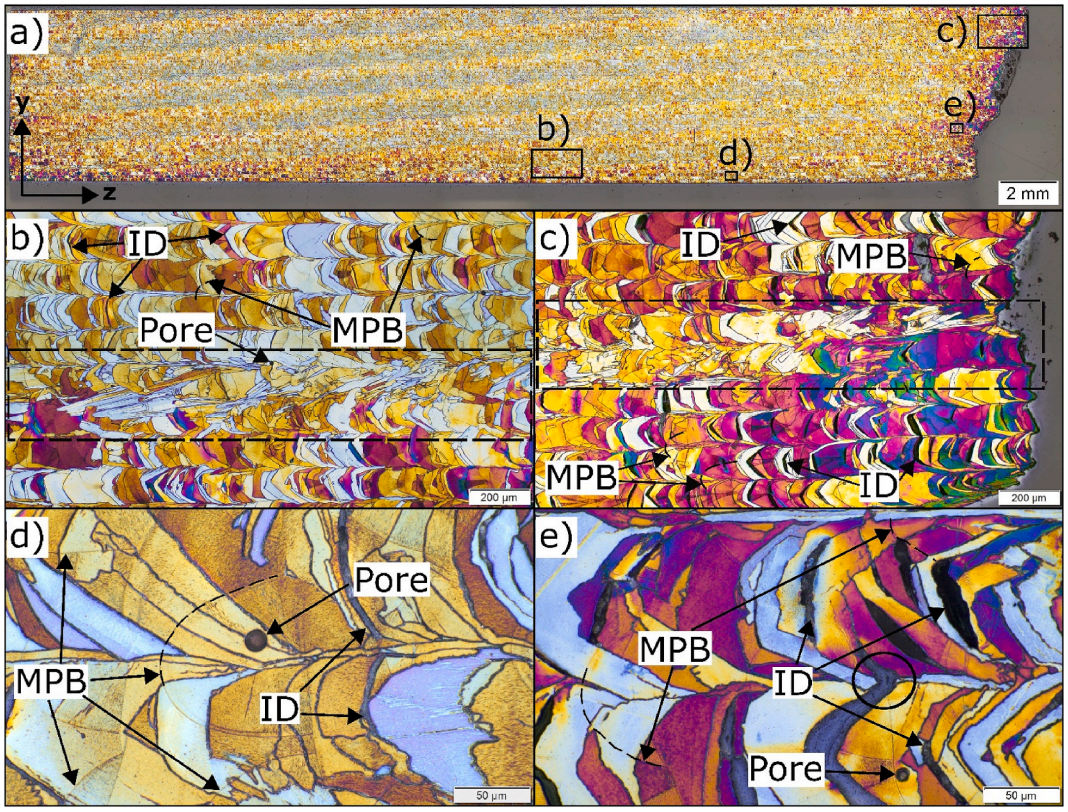

Fig. 11. LPBF creep test piece after failure. OM after etching, same test piece as in Fig. 9. Test parameters are 600 °C/225 MPa, z-coordinate corresponds to the building and loading direction, the coordinate system is the same for all images. a) Overview of cut section, b) and d) Detail views from regions away from the fracture surface, c) and e) Detail views from the vicinity of the fracture surface.

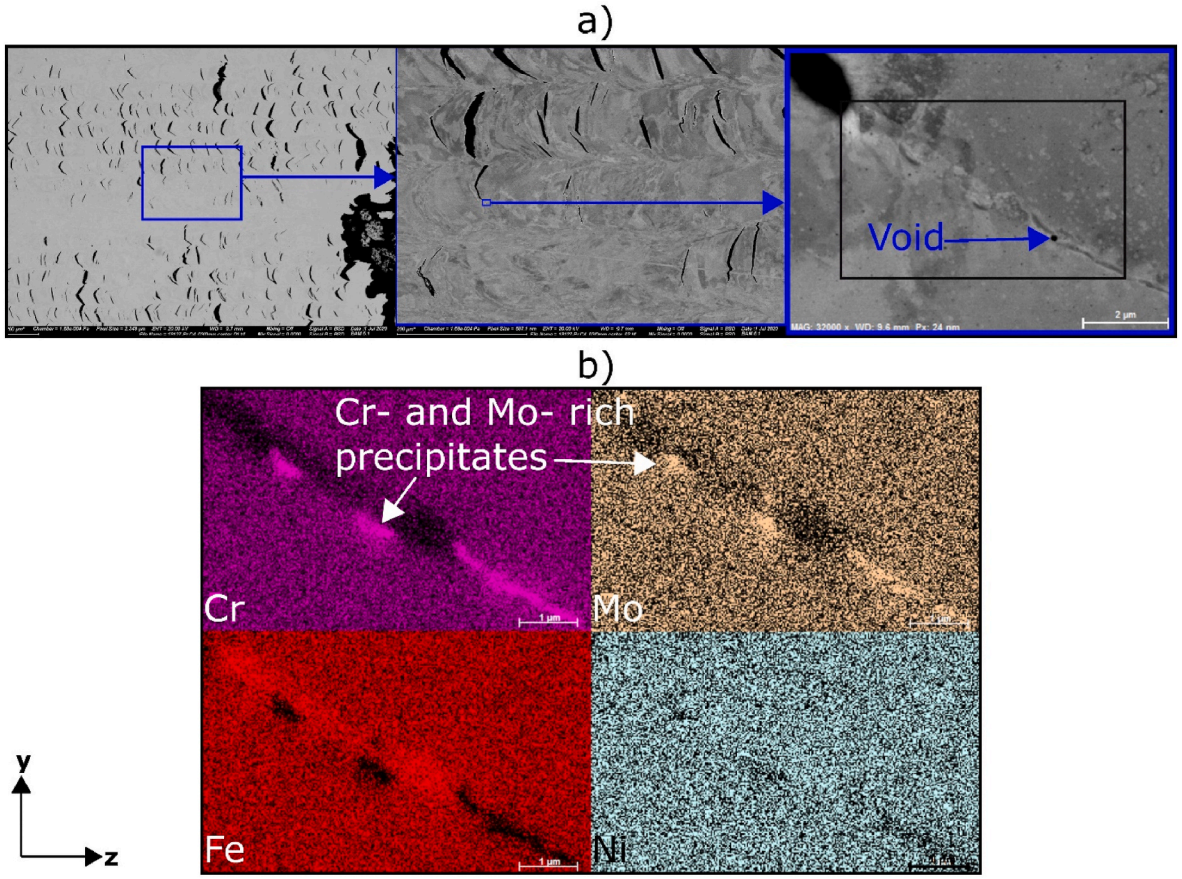

Fig. 12. EDS analysis at crack tip of fractured LPBF creep sample (same as shown in Fig. 9, Fig. 10, and Fig. 11). The coordinate system on the bottom left of the figure applies for all images in the figure. Fig. 12a) BSE Images showing the location of the analyzed crack tip within the cut section. Fig. 12b) Element maps resulting from the EDS measurement for four selected elements. The maps are generated from the location shown with a black box in the rightmost image of Fig. 12a.

condition before testing.

4. Discussion

4.1. Microstructure and tensile strength

The hierarchical microstructure observed in this study for LPBF 316L is a characteristic feature consistent with those reported in literature, e.g. [25,26,50]. In agreement with literature, apart from high and low angle grain boundaries, the microstructure after solidification is characterized by a pronounced cellular structure, which has been reported for several others AM metals [21,25,27,51]. The almost dislocation-free cell interior as well as the cell size observed in our material (Fig. 2) matches well with values reported in the literature [9,25–27,52]. It is well known that this characteristic microstructure resulting from the LPBF process leads to a considerably higher yield strength at room temperature compared to conventional 316L material [9,25,27,53,54]. Besides, it is known that the observed strength of the LPBF material is a combination of several strengthening mechanisms, whereby the cellular structure and associated dislocations play an important role [25,27,55].

Elevated temperatures can potentially destabilize and cause to disappear the cellular structure, thus potentially altering the hot tensile and creep properties. This phenomenon can, in principle, occur during targeted heat treatments or the heat-up of the material before testing at elevated temperatures. In our study, as mentioned in section 3.1, the heat treatment (450 °C/4 h) did not cause any major changes in the as-built microstructure across all length scales. The cellular structure remained stable. The stress relief effect (as-built vs. heat-treated rectangular prisms) was minor (less than 5%) as described by Sprengel et al. in [56]. The subsequent manufacturing of tensile test pieces led to a stronger stress relief effect than the heat treatment [30]; the stresses within test pieces are 10–20% from stresses in rectangular prisms. It is, therefore, reasonable to assume that the cellular structure remains present at least at the beginning of both the hot tensile and the creep tests and that it still plays an important role in the strengthening of the alloy at the tested temperatures. These facts agree well with literature, where in general it has been reported that temperatures (800–900 °C) higher than 450 °C (our heat treatment) or 600–650 °C (our mechanical tests) are needed to cause changes in the microstructure, residual stresses, and room temperature tensile strength [27,52,55–62]. Besides, the drop in the yield strength has been thereby often related to the decrease in the dislocation density associated with the disappearance of the cellular structure. Indeed, the results from our hot tensile tests on the LPBF material (Table 2) coincide roughly with data from Dryepondt et al. [52] and Akino et al. [57].

4.2. Creep behavior

4.2.1. Time to rupture

Fig. 13 compares times to rupture data from several authors on conventional and additively manufactured 316L(N) with the data of Fig. 5. The hot yield strengths (see Table 2) are shown as horizontal lines. Because of the higher hot yield strengths of the LPBF compared to the HR material, it becomes clear that the HR material was loaded in the creep tests above and the LPBF below its hot yield strength (see horizontal lines in Fig. 13; black: LPBF and blue: HR). Testing applied stresses above the hot yield strength (HR material) is questionable from a practical perspective since creep-critical parts, as a rule, should

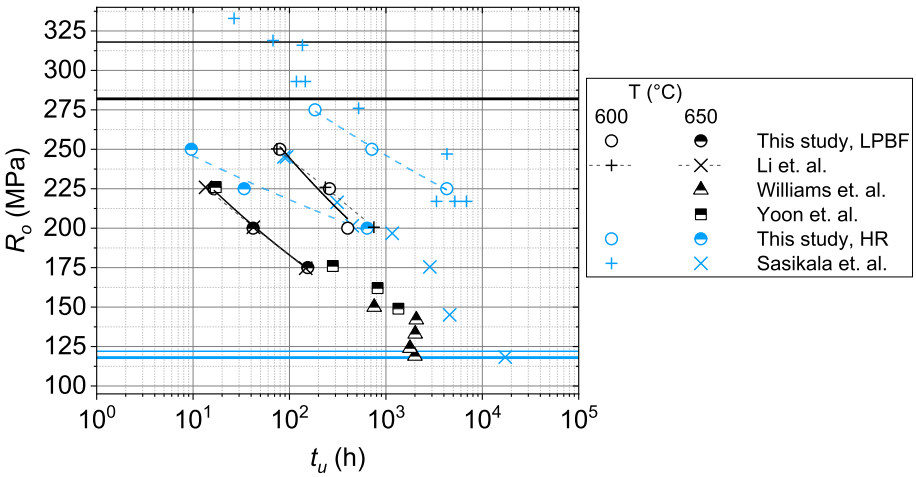

Fig. 13. Rupture times in comparison with literature data.

undergo as little plastic deformation as possible. However, the stresses chosen are commonly used in literature, lead to reasonable rupture times, and permit a comparison to available creep lifetime literature data.

The rupture times from conventionally manufactured 316LN with 0.086 wt % N from Sasikala et al. [14] (blue cross-marks and x) agree very well with the results in our study, taking into account the slightly different nitrogen content. The creep rupture times reported by Li et al. [9] for LPBF 316L (black crosses and cross-marks with dashed lines) agree very well with the results of this study. Besides, our data seem to follow the tendency of the rupture lives of the vertical specimens of the study of Williams et al. [12] (black semi-filled triangles) despite of the different stress states present in notched test pieces. The same tendency is also observed when comparing to the rupture times of the small vertical test pieces of Yoon et al. [11] (black semi-filled squares).

4.2.2. *Creep mechanisms*

The shorter rupture times and the shorter duration of each creep stage, particularly from the primary creep stage may represent a disadvantage of the LPBF material over the HR material. The shorter duration of the individual creep stages and the lower creep ductility are caused by different creep mechanisms of the LPBF material compared to the HR variant. In this subsection, creep deformation and creep damage mechanisms are systematically discussed in separate subsections, although they jointly contribute to the creep behavior of the material.

4.2.2.1. Deformation. The deformation mechanism is understood in this article as the mechanism governing the initial loading and the primary creep. The secondary creep stage is assumed to be partly governed by the deformation mechanism due to competing mechanisms of hardening and recovery. The relative position of the applied stresses with respect to the hot yield strengths for both materials (see Fig. 13) explains the lower initial loading strain and its lower stress dependency, Fig. 3a, as well as the mainly elastic initial response, Fig. 3b, in the LPBF material. This result agrees well with an observation of Wilshire and Willis [20] that pre-straining at room temperature of conventional 316H creep test pieces reduces the initial loading strain to almost zero when crept at 575 °C. They also found that the initial loading strain becomes independent of the applied stress if the pre-strain is high enough to eliminate the plastic component of the initial loading strain. This finding is similar to the behavior of our LPBF material. The small temperature dependency of e_{ti} in both materials, Fig. 3a, can be caused by similar elastic responses independent of the temperature. Similar elastic responses are indeed present and become evident in a plot of the strain response of the materials to the application of load until the initial stress R_o is reached (not shown).

The duration (Fig. 6a and b) and the ductility during the primary creep stage (Figs. 4c and 7) can be affected by several factors. In the following paragraphs, they are systematically discussed. The dislocation substructure is considered one of several controlling factors [9,14]. In the case of the LPBF material, it is organized in cell walls with high dislocation density that are a typical feature of the cellular structure, Fig. 2. The dislocation substructure of the LPBF material resembles a microstructural condition similar to that which forms during dislocation-dominated creep in single-phase crystalline materials during the primary creep stage, which fully develops in the secondary creep stage [63]. Therefore, it is reasonable to argue that the LPBF material does not need much time -and strain-to form the typical microstructure -in terms of dislocations substructure-from the end of a primary creep stage. Besides, this substructure matches the microstructural condition of a cold-worked material (dislocation densities in the order of 10^{14} to 10^{16} m^{-2} were reported for LPBF 316L [21,55]). This condition can limit the strain hardening capacity of the material and thus cause shorter primary creep stage in the LPBF material compared to the HR material. Finally, other authors coalesce around the idea that either the subgrains along with the high dislocation density in 316L weld metal [14] or the dislocation cell structure in the as-built LPBF 316L [9] limit the work-hardening capacity of the material and is therefore responsible for achieving the minimum creep rate faster and at lower strains.

On the other hand, the HR material is characterized by a low dislocation density in the initial state (Fig. 2). It has therefore more hardening capacity than the LPBF material. When the external creep stress is applied, the dislocation density increases gradually with the external stress. In the primary creep region, more dislocations are generated than are removed by recovery. The increasing dislocation density would produce a more tightly meshed dislocation network and thus more significant mutual interference of dislocation motions. At the end of the primary creep stage, an equilibrium between dislocation generation and recovery is established. However, until this is reached, significantly higher creep strain values are achieved compared to the LPBF variant (Fig. 7). Because of the reasons mentioned in the former paragraph, including the supporting literature data, and since the dislocation substructure is a microstructural feature that differs significantly between the two materials studied, it is considered the main factor determining the creep deformation mechanism during the primary creep stage. The future study of heat-treated states of the LPBF material and intermediate states in both materials, e.g. at the end of the primary creep stage, should help to confirm this hypothesis in further studies.

Apart from the dislocation substructure, other factors have been identified in literature to potentially affect the creep deformation mechanism in 316L(N). These factors are primarily related to the chemistry and the phases of the material. The stacking fault energy

(SFE), which is related to the chemical composition, the interstitials (in particular C and N) and its influence on the precipitation behavior, and the presence of delta ferrite count among them. In this work, both materials have nearly the same carbon content, see Table 1, and the LPBF material in this study does not have delta ferrite. Therefore, is assumed that they do not determine the differences in the creep deformation behavior. The presence of nitrogen can increase the duration of the primary and secondary creep stages, Already small differences of ca. 0.04 wt % may play a role, for details see e.g. [14–17,64–66]. In this study, the LPBF material has 0.077 wt % N, which is a higher amount of nitrogen than the HR, and still, it has shorter primary and secondary creep stages. This observation suggests that nitrogen also does not play a major role in determining the different creep deformation behaviors between the two materials.

Finally, the SFE is widely believed to be an important parameter influencing the high-temperature deformation behavior of metallic materials. Sherby and Burke [67] describe this correlation in a qualitative manner. When the SFE is reduced, the distance between partial dislocations is increased since it is easier to create the stacking fault between the partials. The widely extended dislocations have then difficulty climbing because the partials must first combine before climb becomes possible. The more widely separated the dislocations (lower SFE), the greater the difficulty in climb (recovery process), and hence the creep rate is reduced proportionally. The increased difficulty in the recovery process leads potentially to longer durations of the primary and secondary creep stages [67]. However, interpretations must be taken with care, since at elevated temperatures, where creep occurs, the apparent value of the SFE increases, and a correlation between high-temperature creep rate and room temperature SFE of alloys is questionable, see [68].

The SFE can be quantitatively determined by TEM investigations involving extensive amounts of work. In our case, for comparison purposes, it is estimated based on the chemical composition using the formula proposed by Schramm et al. [69] for austenitic steels, eq. (6). That formula considers the content of the impurities and interstitials such as C, N, Si, P, S, Co, etc. and of Ni, Cr, Mn and Mo. The influence of the interstitials is represented presumably by the negative constant at the beginning of the equation [69].

$$SFE\left(mJ/m^2\right) = -53 + 6.2\ wt\ \%\ Ni + 0.7\ wt\ \%\ Cr + 3.2\ wt\ \%\ Mn + 9.3\ wt\ \%\ Mo \quad (6)$$

Based on eq. (6), the SFE of the LPBF material is 62.9 mJ/m^2 and that of the HR material is 44.4 mJ/m^2, i.e., the estimated SFE is lower in the HR material compared to the LPBF variant. This agrees well with the presence of more partial dislocations in the HR material than in the LPBF variant (Fig. 2). This lower SFE of the HR material can potentially be the cause of the longer durations of the primary and secondary creep stages. Conversely, the higher SFE of the LPBF material, in addition to its cellular structure, can be considered as a possible -secondary- cause for the shorter primary and secondary creep stages compared to the HR material, provided that the SFE of the HR material remains lower than that of the LPBF material at the test temperatures.

4.2.2.2. Damage. The general understanding of creep damage is that it governs the secondary and tertiary creep stages [70]. The damage mechanism governs the tertiary creep and the secondary creep. During secondary creep, the mechanisms that originate the formation of damage and cause the onset of tertiary creep can already appear. The onset of tertiary creep represents the initiation of conditions that lead to fracture and is an indication that voids or cracks are slowly but continuously forming in the material [71]. The microcracks, present primarily within the columnar regions, play a major role in the mostly intergranular failure of the LPBF material, as evident in the fracture surfaces and cut sections shown in Figs. 9, Figure 10, and Fig. 11. The ductile fracture present in the intercolumnar regions (see Fig. 10) contributes to a minor extent to it. The microcracks presumably determine the duration of the tertiary creep (Fig. 6c) and partly also the lower ductility of this alloy compared to the HR variant (Fig. 4c). During tertiary creep, the microcracks might be detectable. Further investigation of interrupted conditions should help clarify the time course of cracking, and whether the mechanisms causing it starts already in the secondary creep. In the following paragraphs, first, the nature of the damage of the two investigated materials and, subsequently, the different factors or mechanisms that may contribute to the formation of the microcracks in the LPBF material are discussed.

The damage of the LPBF test piece is characterized by the intergranular creep damage shown in Figs. 9 and 11, which develops along the grain boundaries. The final fracture is overall mainly intergranular. Our results contrasts with the results of Williams et al. [12] and are in agreement with the work of Li et al. [9], disregarding the different grain morphologies. The rather ductile-like fracture in the intercolumnar regions (Fig. 10) suggests that more deformation accumulates in these regions during the creep test. In our almost defect-free investigated LPBF material's test piece (porosity less than 0.01%), the gas pores did not play a role in the damage behavior and did not interact with or enhance the microcrack formation. This enabled us to evaluate microstructure towards the damage behavior, excluding porosity and lack of fusion defects. The μCT and optical microscopy results presented in Figs. 9 and 11 show that the microcracks in the LPBF creep test piece occur mainly at the grain boundaries that are oriented either 45° tilted to the loading direction, the theoretical region of maximum shear stress, or perpendicular to it. This differs slightly from the results of Williams et al. [12] where creep cavities were seen at grain boundaries oriented perpendicular as well as nearly parallel to the building direction. In contrast to the LPBF test piece, the HR test piece is characterized by ductile transgranular fracture typical of creep tests at high stresses near the hot tensile strength [72], and fracture occurs with significant necking.

The large amount of unfavorable oriented grain boundaries is evidently one of the mechanisms that can accelerate the intergranular damage of the LPBF material since the unfavorable orientation of the grain boundaries is known to be detrimental to the creep damage behavior [29]. However, as evidenced in Figs. 1 and 8, the HR material has as well a large amount of grain boundaries that are unfavorable oriented and still has considerably less intergranular damage. The different deformation and damage characteristics could help explain it: as evident from the results of the creep tests (see Table 3, Figs. 3, Figure 7), the HR material can deform more during the creep loading, because it has more hardening capacity in the initial condition, as discussed in subsection 4.2.2.1. Besides, in contrast to the LPBF material, microcracks do not form at the grain boundaries (see Fig. 8 vs. Fig. 11), thus allowing the grains to deform more before failure.

In addition to the unfavorable oriented grains, the appearance of the precipitates seen in Fig. 12 might be a process that weakens the grain boundaries and thus be a further triggering and accelerating factor for the intergranular damage. These precipitates, based on a time-temperature-precipitation (TTP) diagram of the conventional variant of this material, see [75], and the results on wrought material of Sasikala et al. [14] the precipitates could be $M_{23}C_6$-type carbides. As the results in subsection 3.3.2 suggest, the appearance of these precipitates might be a process that weakens the grain boundaries and triggers and accelerates the intergranular damage. In fact, grain boundary precipitates are by far considered as the most important crack nucleation sites during creep cavitation of creeping alloys [74]. Apart from the existence of the precipitates per se, the different precipitation characteristics can cause the different damage behaviors between the two materials. Indeed, it is known that if carbides form in austenitic stainless steels, their density, the maximum intercarbide spacing might play a role in the damage caused [73]. In our study, the precipitates in the LPBF material were mainly at grain boundaries and in general much smaller and more often seen than in the HR material (see subsection 3.3.2, Fig. 12).

The small voids observed rather rarely along the grain boundaries in

the outgoing condition and more often in the crept test pieces near crack tips (see Fig. 12) and at grain boundaries might also play a role in the formation of cracks. These small voids can be either gas pores, which may act as crack initiation sites, or round-type (r-type) cracks or cavities in different formation states. The formation of r-type cracks is usually observed in intergranular creep damage [29,76]. These cavities can form either by the accumulation of vacancies under an effective tensile stress or by a change in the bonding states in the material [77]. Apart from r-type cracks, wedge-type (w-type) cracks are usually observed in intergranular creep damage [29,76]. The relative movements of the grains along their grain boundaries cause stress concentrations at grain boundary triple points, grain boundary steps, and grain boundary particles [29]. If these stresses are not or only incompletely relaxed in the grain volume, crack initiation occurs at those locations. The latter formation mechanism could also potentially contribute to the formation of the microcracks observed in this study in the LPBF material.

Another interesting aspect worth investigating as a contributing factor to the creep damage is the influence of a quasi-predeformed state in the LPBF material, which is caused by the dislocation substructure (Fig. 2). It is reported in the literature [29] that previous deformation at room temperature favors the formation of creep voids and increases their number. In conventionally manufactured materials, the spacing of the cavities is associated with the spacing of slip bands. This fact opens the question of whether or not the very small dimples on the intergranular fracture surfaces of the grain boundaries (Fig. 10) are associated with the dislocation cell structures present in the LPBF material. Detailed TEM and SEM studies should help to test this hypothesis in further studies.

Further postmortem investigations reveal that the cellular structure remains present after the creep tests in the same sample investigated (Fig. 14). The cellular structure appears as rough features over the whole surface in the SEM image after etching. The features represent protrusions due to micro-segregation at the cellular boundaries [21] and do not necessarily evidence the existence of the dislocation substructure (Fig. 2) after testing. Li et al. [9], however, demonstrated its existence and instability after creep at 550 °C and 650 °C. This observation opens the ground to discuss whether it plays a role in the damage behavior since it still exists in the material after failure. Due to the nature of the cellular structures in LPBF metals, one can argue that it may be able to accelerate the onset of the tertiary creep stage. Indeed, apart from the high concentrated dislocation density, the cell walls feature segregation of nanoparticles and enrichment of chromium and molybdenum along them. The characteristic enrichment of chromium and molybdenum along the cell walls can potentially accelerate the precipitation process at the grain boundaries of the LPBF material compared to the HR variant. This can be the case if, for instance, a high concentration of cell walls is randomly located near or exactly at a grain boundary.

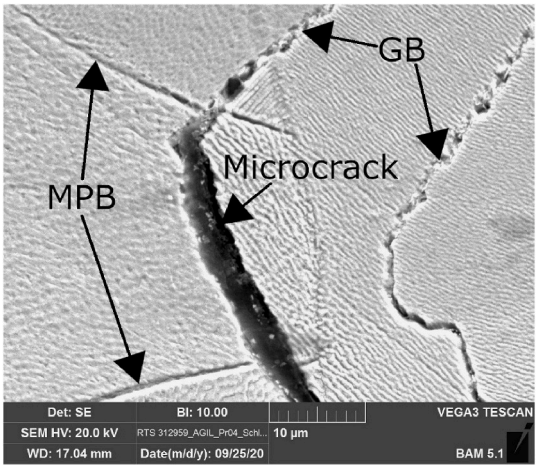

Fig. 14. SE SEM image in etched state of a region near to a microcrack in the LPBF material. The cellular structure remains present after the creep tests. Partially cracked grain boundaries (GB) and melt pool boundaries (MPB) are visible.

Finally, the local solidification conditions of the AM process cause a local variation of the relative orientation of the slip systems to the loading direction. This local variation in the relative orientation of the cells and therefore of the slip systems to the loading direction might as well be a contributing factor for the formation of damage. The epitaxial growth occurs perpendicular to the MPBs, causing that within a grain, the cells grow in different directions to the sample's coordinate system, following the preferred local crystal growth direction, in fcc crystal <001> [21,79]. The MO-angle used to define the grain size in this article (15°) was chosen to make the grain size roughly consistent with the grain boundaries that are seen in Fig. 1. This decision implies that within one grain there are zones that consist of cell colonies with different orientations. The biggest orientation difference is present in cells growing from the bottom of the MPBs, which contribute to a crystallographic weak {100} texture vs. crystals not growing from it, which determine the predominant {110} crystallographic texture of the material, reported by Charmi et al. [30]. In the intercolumnar regions (cells growing from the bottom of the MPBs), the <001> directions of the fcc unit cell will tend to become parallel to the loading direction. Towards the middle region of the columns of grains, they will tend to become perpendicular to it. Accordingly, depending on this change of the relative orientation of the columnar cell structures to the loading direction, different slip systems will become differently active as the Schmid factor varies, tending to be higher in the intercolumnar regions.

From the discussion in this subsection 4.2.2, it is clear that further investigations are needed to better understand the creep deformation and damage mechanisms. These investigations should include interrupted creep tests accompanied by microscopy and μCT to understand the sequence of damage development and dedicated TEM investigations to elucidate the role of cellular structure. These detailed studies are planned but are way beyond the scope of this article.

4.2.3. *Dependency of minimum creep rate on stress*

The creep rate is an important design parameter, and information such as the stress to produce a specific creep rate is usually determined from the test data. The creep rate depends on the applied stress and temperature. It is well known that in the medium stress range (as studied here), the stress dependency of the secondary creep rate follows a power law, eq. (7) with reasonable accuracy [80].

$$\dot{e}_s(\sigma) = C \cdot (R)^n \tag{7}$$

A logarithmic representation of the creep rate vs. stress for a given temperature can be fitted to a line, eq. (8).

$$\log \dot{e}_s = \log A + n \log R \tag{8}$$

The slope of that line represents the stress exponent, n, and defines the dependency of the minimum creep rate on the stress at a given test temperature. In the case of simple model materials (e.g. pure metals), n, can be interpreted in terms of the steady-state creep approach, which is based on the physical view that a strain hardening process (e.g., increase of dislocation density) is balanced by a thermal recovery process (e.g., climb-controlled dislocation annihilation) resulting in a dynamically steady microstructure (e.g. with constant dislocation density) [29]. A stress exponent of 3–5 is for model materials (e.g. pure metals, binary alloys) associated with recovery-creep processes controlled by diffusion [68,81]. For technical alloys, however, the exponents can be significantly higher. Besides, as mentioned in [68], the determination of n in limited domains of stress and temperature do not provide enough information to pinpoint the creep processes. It has little physical significance per se and cannot be used to discriminate between mechanisms. Thus, interpretation of the exponents in terms of the deformation

mechanism may not be meaningful without a detailed microstructure investigation. Therefore, the values for n are determined here for the literature comparison but are not interpreted further in terms of creep mechanisms.

The stress exponents calculated using the initial stress, R_o, as R in eqs. 7 and 8, n_o, are shown in Table 4 and Fig. 15. The calculation using R_o allows for a comparison with literature data. Since the tests in this study are performed under constant force, the stress increases with increasing test duration and total strain as the cross-section of the test piece reduces. This means that at the point when the minimum creep rate is reached, the actual stress is higher. The latter is particularly the case in the HR material, which experiences a greater reduction of area, as evidenced by the values after rupture, Z_u, in Table 3. The actual stresses at minimum creep rate, R , can be calculated according to eq. (9) for each test.

$$R = R_o(1 + e_{ti} + (e_f \ at \ \dot{e}_s)) \tag{9}$$

Using R, one can recalculate the stress exponents, n, which are also shown in Table 4. As expected, due to the lower reduction of area in the LPBF material, its stress exponents do not differ significantly. In the HR material, the n-values are, on average, 10% lower than the n_o-values. The actual stresses at minimum creep rate in the HR material are, on average, 20 MPa higher than the applied stresses, whereas in the LPBF material R_o and R are almost equal. A correction of the applied stress does not affect the comparative analysis of the creep behavior between the two investigated materials despite the reduction of area of the HR variant.

The dependency of the minimum creep rate on the applied stress is shown in Fig. 15 for both tested materials and temperatures along with literature data. Table 4 and Fig. 15 show that the LPBF material (black open and semi filled circles) has smaller stress exponents (6.5 or 8.2) compared to the HR material (17.6 or 19.3; blue open and semi filled circles). The stress dependency of the minimum creep rate is weaker in the LPBF material. Besides, Fig. 15 shows that at each tested temperature, the minimum creep rates of both materials can be similar for the same applied stresses, where a comparison is possible, e.g., at 600 °C/250 MPa and 650 °C/200 MPa. However, this seems to be stress dependent. Furthermore, Table 4 and Fig. 15 show that increasing the temperature increases slightly the stress exponents for both materials. When comparing to literature data, the stress exponents of the LPBF material are tendentially smaller than the comparison data, except for Williams et al. [12]. The minimum creep rates of the LPBF material of this study are at least one order of magnitude lower than the literature data. Concerning the HR material, they are also almost one order of magnitude lower, and the stress exponents higher.

Wilshire and Willis [20] pointed out that microstructure variations (e.g., due to partial solution heat treatment) may result in a large scatter of results. They reported $n = 8$ for T = 575 °C, both for a solution annealed conventional 316 stainless steel and for the same material prestrained at room temperature. It is, therefore, expected that the differences in the microstructure may partly explain the differences in stress exponents of this study when compared to literature data. In the study of Sasikala et al. [14], the material was tested in the solution-annealed condition, contained delta-ferrite in an austenitic matrix, and had an equiaxed grain structure with a mean-linear intercept grain size of 88 μm (against 30 μm in our case). The cell sizes reported by Li et al. [9] and Yoon et al. [11] in LPBF 316L are similar to the those shown in this study. In contrast, the columnar grain morphology, similar between their studies and the study of Williams et al. [12], differs from that reported in this study. The grain morphology in [9,11,12] does not feature the "ripple-like" shape visible in Fig. 1, and the grains' shape seems to be more like those of the intercolumnar region of this study. In addition, the difference in nitrogen content might play a role. Mathew et al. [17] showed that increasing the nitrogen content leads to smaller stress exponents. The difference in nitrogen contents could partly explain the higher stress exponents of the results of the HR material of this study (0.045% N) if compared to Sasikala et al. [14] (0.086 wt % N), and the smaller stress exponent of the LPBF material of this study (0.077% N) if compared to the data of Li et al. [9] (0.067 wt % N).

The similarity in minimum creep rates at some stress levels, e.g., at 600 °C/250 MPa and 650 °C/200 MPa, suggests that a similar dislocation substructure can be reached in both investigated materials, on the assumption that the HR material tends to develop a substructure as described by Takeuchi et al. [63]. The smaller stress exponents (lower stress dependency of the minimum creep rate) of the LPBF compared to the HR material further supports the hypothesis mentioned in section 4.2.2 that the dislocation substructure associated to the cellular structure is the main contributor to the minimum creep rate and, therefore, the creep strength in the LPBF material. Indeed, building on the latter ideas, it is conceivable that at higher stresses or shorter exposures, the HR material cannot form a dislocation substructure similar to that in the LPBF material. At lower stresses or longer exposures, it might develop a finer one.

4.3. Improvement opportunities

The LPBF material studied did not have a microstructure optimized for creep or intended to represent a material to be applied in real applications. It instead allows for the isolated study of the effect on the creep behavior of other aspects of a typical LPBF microstructure, e.g., the cellular structure or the grain morphology. Based on the results and previous discussion, some opportunities to improve the creep behavior through microstructure modifications are presented in the following paragraphs.

Since the cellular structure is considered to play an important role in the creep mechanisms, one would like to partly dissolve it as an approach to improve the creep properties of the LPBF material. The use of targeted heat treatments that dissolve it to some extent, especially the associated dislocation substructure, while not changing the microstructure drastically is crucial. Some work has been already published addressing this topic, e.g. [55,82,83], however mostly only room temperature tensile properties have been investigated (see section 4.1). Apart from diminishing the initial dislocation density, targeted post-processing strategies or even targeted process variations can avoid

Table 4
Stress exponents calculated according to eq. (8) using initial applied stress, R_o, and the actual stresses at the minimum creep rate stress, R, respectively resulting in exponents n_o and n.

		LPBF						HR					
T	°C	600			650			600			650		
Test piece no.	–	1	2	3	1	2	3	1	2	3	1	2	3
R_o	MPa	200	225	250	175	200	225	225	250	275	200	225	250
R		201	226	251	176	201	226	240	270	302	218	243	276
n_o			6.5			8.2			17.6		19.3		
n			6.5			8.3			15.3		17.9		

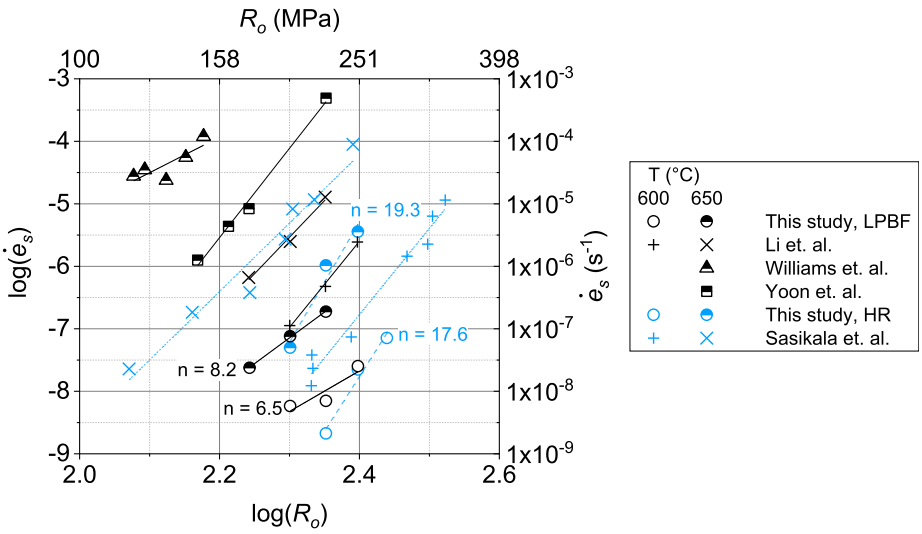

Fig. 15. Minimum creep rate vs. applied stress, literature data for comparison is included.

or eliminate chromium and molybdenum segregation along the cell walls. For some work in this direction with other alloys, see e.g. [84,85].

Modifying the chemical composition and with it the SFE, also represents an improvement opportunity, see eq. (6). Slightly reducing the contents in Ni, Cr, Mn, and Mo, while remaining within the limits of the specification [36], could help to decrease the SFE and thus increase the duration of the primary and secondary creep stages. Changing the content in interstitials and impurities is, however, rather not conceivable. On the one hand, in eq. (6), the exact compositional dependencies of the interstitials and impurities are unknown, and a significant second-order effect on SFE composition dependence is presumed [69]. On the other hand, the impurities and interstitials can hardly be controlled in the AM process.

Other potential improvement opportunities are to change the loading direction relative to the grain morphology or to change the grain morphology itself, e.g., through partial recrystallization. The latter can be done by tailoring the LPBF process or through heat treatments, targeting an optimal balance of properties. However, on changing the loading direction by 90° while maintaining the same grain morphology, all the grain boundaries in the intercolumnar regions would become perpendicular to it, and the 45° oriented grain boundaries would remain at the same angle. This approach could thus possibly lead to similar or even worse results. Finally, since the grain boundaries appear to be inherently weak, techniques that strengthen the grain boundaries such as grain boundary engineering (GBE) are an interesting approach [86].

5. Conclusions

In this study, a thorough characterization of the creep behavior of LPBF 316L contributing to the sparse available data is presented in comparison to its wrought counterpart. Hot tensile tests and creep tests at 600 °C and 650 °C are performed. Furthermore, supported by targeted microstructural investigations, a first step is taken towards understanding the evolution of the microstructure and the main underlying factors governing the creep deformation and damage mechanisms. The most relevant conclusions are:

- The LPBF material has a unique creep deformation behavior. The stress dependency is lower than in the HR material. In terms of ductility, it features smaller initial loading strains, e_{ti}, and creep strains, e_f, and reaches the minimum creep rate at significantly lower creep strains, around one decade lower, compared to the wrought counterpart at all tested combinations of parameters. The LPBF material has shorter times to rupture, shorter primary and secondary creep stages, and a shorter tertiary creep stage than the HR material at all combinations of test parameters. The cellular structure is considered to be the main cause of the differences in deformation behavior, especially during the first creep stage, primarily because it limits the work hardening capacity of the material. The higher SFE presumably also plays a role. The difference in nitrogen contents is of no significance.
- The final fracture in the LPBF material is overall mainly intergranular in contrast to the HR material. There are zones that feature intergranular brittle-like fracture as well as zones that show a rather ductile fracture. The zones with a brittle-like fracture are located towards the middle of the columns of grains, where the grain boundaries are more perpendicular to the loading direction. The regions of the material where the grain boundaries are rather parallel to the loading direction, which coincide with the location of the bottom of the MPBs, feature a rather ductile failure suggesting that they bear the most deformation.
- The intergranular damage leads to cracking and subsequently to the failure of the material. It is presumably caused and accelerated by both the appearance of precipitates at the grain boundaries that seemingly weakens them and their unfavorable orientation. The dislocation substructure is also a factor that might play a role in triggering or accelerating the intergranular damage. As evidenced in Figs. 9 and 11, neither the melt pool boundaries nor the larger intragranular gas pores significantly influence the creep damage mechanism.

Data availability

The raw/processed data required to reproduce these findings cannot be shared at this time as the data also forms part of an ongoing study.

Funding

This work was supported by the BAM focus area materials project AGIL “Microstructure development in additively manufactured metallic components: from powder to mechanical failure”.

CRediT authorship contribution statement

L.A. Ávila Calderón: Conceptualization, Methodology, Validation, Formal analysis, Investigation, Writing – original draft, Writing – review & editing, Visualization. **B. Rehmer:** Conceptualization, Methodology, Writing – original draft, Supervision. **S. Schriever:** Formal analysis,

Investigation, Writing – review & editing. **A. Ulbricht:** Formal analysis, Investigation, Writing – review & editing. **L. Agudo Jácome:** Conceptualization, Investigation, Visualization, Investigation, Writing – original draft, Writing – review & editing. **K. Sommer:** Investigation, Writing – review & editing. **G. Mohr:** Investigation, Writing – review & editing. **B. Skrotzki:** Conceptualization, Methodology, Writing – review & editing, Supervision. **A. Evans:** Conceptualization, Writing – review & editing, Supervision, Project administration.

Declaration of competing interest

The authors declare that they have no known competing financial interests or personal relationships that could have appeared to influence the work reported in this paper.

Acknowledgments

The authors thank Dr. rer. nat. Sebastian Recknagel (BAM-1.6) for determining the chemical composition, Dr.-Ing. Pedro Dolabella Portella and Prof. Dr. Robert Maaß (BAM-5) for stimulating discussion, Elke Sonnenburg (BAM-5.1) for her collaboration in sample preparation, metallography, optical, and electron microscopy, Romeo Saliwan Neumann (BAM-5.1) for his collaboration in electron microscopy (EBSD) and spectroscopy (EDS), and Kathrin Ohm (BAM-9.1) for her collaboration in optical microscopy.

References

[1] J.O. Milewski, Additive manufacturing of metals: from fundamental technology to rocket nozzles, Medical Implants, and Custom Jewelry, Additive Manufacturing of Metals 258 (2017) 1–343.
[2] G. Liu, X. Zhang, X. Chen, Y. He, L. Cheng, M. Huo, J. Yin, F. Hao, S. Chen, P. Wang, S. Yi, L. Wan, Z. Mao, Z. Chen, X. Wang, Z. Cao, J. Lu, Additive manufacturing of structural materials, Mater. Sci. Eng. R Rep. (2021) 100596, https://doi.org/10.1016/j.mser.2020.100596.
[3] N. Hrabe, N. Barbosa, S. Daniewicz, N. Shamsaei, Findings from the NISTASTM Workshop on Mechanical Behavior of Additive Manufacturing Components, National Institute of Standards and Technology, Gaithersburg, MD, 2016.
[4] T. DebRoy, H.L. Wei, J.S. Zuback, T. Mukherjee, J.W. Elmer, J.O. Milewski, A. M. Beese, A. Wilson-Heid, A. De, W. Zhang, Additive manufacturing of metallic components - process, structure and properties, Prog. Mater. Sci. 92 (2018) 112–224, https://doi.org/10.1016/j.pmatsci.2017.10.001.
[5] W.2 AD 2000-Merkblatt, Austenitic and Austenitic-Ferritic Steels, Deutsches Institut für Normung e. V., Beuth Verlag, Berlin, 2020-01.
[6] R. Baldev, U. Kamachi Mudali, M. Vijayalakshmi, M.D. Mathew, A.K. Bhaduri, P. Chellapandi, S. Venugopal, C.S. Sundar, B.P.C. Rao, B. Venkatraman, Development of stainless steels in nuclear industry: with emphasis on sodium cooled fast spectrum reactors history, technology and foresight, Adv. Mater. Res. 794 (2013) 3–25. https://doi.org/10.4028/www.scientific.net/AMR.794.3.
[7] A. Stanculescu, GIF R&D outlook for generation IV nuclear energy systems: 2018 update, in: 13th GIF-IAEA Interface Meeting Presentations, International Atomic Energy Agency (IAEA), 2019, p. v.
[8] First Installation of a 3D Printed Thimble Plugging Device in Nuclear Plant, 2020. (Accessed 23 September 2020).
[9] M. Li, X. Zhang, W.-Y. Chen, T.S. Byun, Creep behavior of 316 L stainless steel manufactured by laser powder bed fusion, J. Nucl. Mater. 548 (2021) 152847, https://doi.org/10.1016/j.jnucmat.2021.152847.
[10] J.M. Yu, V.H. Dao, K.B. Yoon, Investigation of creep behavior of 316L stainless steel produced by selective laser melting with various processing parameters, J. Mech. Sci. Technol. (2020), https://doi.org/10.1007/s12206-020-0717-z.
[11] K.B. Yoon, V.H. Dao, J.M. Yu, Effects of Build Direction on Tensile and Creep Properties of 316L Stainless Steel Produced by Selective Laser Melting, Fatigue & Fracture of Engineering Materials & Structures, 2020, https://doi.org/10.1111/ffe.13322 n/a(n/a).
[12] R.J. Williams, J. Al-Lami, P.A. Hooper, M.-S. Pham, C.M. Davies, Creep Deformation and Failure Properties of 316 L Stainless Steel Manufactured by Laser Powder Bed Fusion under Multiaxial Loading Conditions, Additive Manufacturing, 2020, p. 101706, https://doi.org/10.1016/j.addma.2020.101706.
[13] M. Rieth, A. Falkenstein, P. Graf, S. Heger, U. Jaentsch, M. Klimiankou, E. Materna-Morris, H. Zimmermann, Creep of the Austenitic Steel AISI 316 L(N) Experiments and Models, 2004, p. 80. Germany.
[14] G. Sasikala, M.D. Mathew, K.B.S. Rao, S.L. Mannan, Creep deformation and fracture behavior of types 316 and 316L(N) stainless steels and their weld metals, Metall. Mater. Trans. 31 (4) (2000) 1175–1185, https://doi.org/10.1007/s11661-000-0113-3.
[15] M.D. Mathew, G. Sasikala, K. Bhanu Sankara Rao, S.L. Mannan, Influence of carbon and nitrogen on the creep properties of type 316 stainless steel at 873 K, Mater. Sci. Eng., A 148 (2) (1991) 253–260, https://doi.org/10.1016/0921-5093(91)90827-A.
[16] M.D. Mathew, S. latha, G. Sasikala, S.L. Mannan, P. Rodriguez, Creep properties of three heats of type 316 stainless steel for elevated temperature nuclear applications, Nucl. Technol. 81 (1) (1988) 114–121, https://doi.org/10.13182/NT88-A34083.
[17] M.D. Mathew, K. Laha, V. Ganesan, Improving creep strength of 316L stainless steel by alloying with nitrogen, Mat Sci Eng a-Struct 535 (2012) 76–83, https://doi.org/10.1016/j.msea.2011.12.044.
[18] Y.M. Arısoy, L.E. Criales, T. Özel, B. Lane, S. Moylan, A. Donmez, Influence of scan strategy and process parameters on microstructure and its optimization in additively manufactured nickel alloy 625 via laser powder bed fusion, Int. J. Adv. Manuf. Technol. 90 (5) (2017) 1393–1417, https://doi.org/10.1007/s00170-016-9429-z.
[19] B. Attard, S. Cruchley, C. Beetz, M. Megahed, Y.L. Chiu, M.M. Attallah, Microstructural control during laser powder fusion to create graded microstructure Ni-superalloy components, Additive Manufacturing 36 (2020) 101432, https://doi.org/10.1016/j.addma.2020.101432.
[20] B. Wilshire, M. Willis, Mechanisms of strain accumulation and damage development during creep of prestrained 316 stainless steels, Metall. Mater. Trans. 35 (2) (2004) 563–571, https://doi.org/10.1007/s11661-004-0367-2.
[21] K.M. Bertsch, G. Meric de Bellefon, B. Kuehl, D.J. Thoma, Origin of dislocation structures in an additively manufactured austenitic stainless steel 316L, Acta Mater. 199 (2020) 19–33, https://doi.org/10.1016/j.actamat.2020.07.063.
[22] W.M. Tucho, P. Cuvillier, A. Sjolyst-Kverneland, V. Hansen, Microstructure and hardness studies of Inconel 718 manufactured by selective laser melting before and after solution heat treatment, Mater. Sci. Eng., A 689 (2017) 220–232, https://doi.org/10.1016/j.msea.2017.02.062.
[23] L.E. Murr, Metallurgy of additive manufacturing: examples from electron beam melting, Additive Manufacturing 5 (2015) 40–53, https://doi.org/10.1016/j.addma.2014.12.002.
[24] L. Murr, Handbook of Materials Structures, Properties, Processing and Performance, 2015.
[25] Y.M. Wang, T. Voisin, J.T. McKeown, J. Ye, N.P. Calta, Z. Li, Z. Zeng, Y. Zhang, W. Chen, T.T. Roehling, R.T. Ott, M.K. Santala, Philip J. Depond, M.J. Matthews, A. V. Hamza, T. Zhu, Additively manufactured hierarchical stainless steels with high strength and ductility, Nat. Mater. 17 (1) (2018) 63–71, https://doi.org/10.1038/nmat5021.
[26] N. Haghdadi, M. Laleh, M. Moyle, S. Primig, Additive manufacturing of steels: a review of achievements and challenges, J. Mater. Sci. 56 (1) (2021) 64–107, https://doi.org/10.1007/s10853-020-05109-0.
[27] Y. Hong, C. Zhou, Y. Zheng, L. Zhang, J. Zheng, The cellular boundary with high density of dislocations governed the strengthening mechanism in selective laser melted 316L stainless steel, Mater. Sci. Eng., A 799 (2021) 140279, https://doi.org/10.1016/j.msea.2020.140279.
[28] L. Cui, S. Jiang, J. Xu, R.L. Peng, R.T. Mousavian, J. Moverare, Revealing relationships between microstructure and hardening nature of additively manufactured 316L stainless steel, Mater. Des. 198 (2021) 109385, https://doi.org/10.1016/j.matdes.2020.109385.
[29] M.E. Kassner, in: Fundamentals of Creep in Metals and Alloys, second ed., Elsevier, Amsterdam, 2008.
[30] A. Charmi, R. Falkenberg, L. Ávila, G. Mohr, K. Sommer, A. Ulbricht, M. Sprengel, R. Saliwan Neumann, B. Skrotzki, A. Evans, Mechanical anisotropy of additively manufactured stainless steel 316L: an experimental and numerical study, Mater. Sci. Eng., A 799 (2021) 140154, https://doi.org/10.1016/j.msea.2020.140154.
[35] G. Mohr, N. Scheuschner, K. Hilgenberg, In situ heat accumulation by geometrical features obstructing heat flux and by reduced inter layer times in laser powder bed fusion of AISI 316L stainless steel, Procedia CIRP 94 (2020) 155–160, https://doi.org/10.1016/j.procir.2020.09.030.
[36] EN 10028-7, Flat Products Made of Steels for Pressure Purposes - Part 7: Stainless Steels; German Version, Deutsches Institut für Normung e. V., Beuth Verlag, Berlin, 2016, 2016-10.
[37] J. Darbon, A. Cunha, T.F. Chan, S. Osher, G.J. Jensen, Fast nonlocal filtering applied to electron cryomicroscopy, in: 5th IEEE International Symposium on Biomedical Imaging: from Nano to Macro, 2008, 2008, pp. 1331–1334.
[38] A.a.C. Buades, Bartomeu and morel, jean-michel, non-local means denoising, Image Process. Line 1 (2011) 208–212, https://doi.org/10.5201/ipol.2011.bcm_nlm.
[39] J. Schindelin, I. Arganda-Carreras, E. Frise, V. Kaynig, M. Longair, T. Pietzsch, S. Preibisch, C. Rueden, S. Saalfeld, B. Schmid, J.-Y. Tinevez, D.J. White, V. Hartenstein, K. Eliceiri, P. Tomancak, A. Cardona, Fiji: an open-source platform for biological-image analysis, Nat. Methods 9 (7) (2012) 676–682, https://doi.org/10.1038/nmeth.2019.
[40] S. Berg, D. Kutra, T. Kroeger, C.N. Straehle, B.X. Kausler, C. Haubold, M. Schiegg, J. Ales, T. Beier, M. Rudy, K. Eren, J.I. Cervantes, B. Xu, F. Beuttenmueller, A. Wolny, C. Zhang, U. Koethe, F.A. Hamprecht, A. Kreshuk, ilastik: interactive machine learning for (bio)image analysis, Nat. Methods 16 (12) (2019) 1226–1232, https://doi.org/10.1038/s41592-019-0582-9.
[41] DIN EN ISO 6892-2, 2018-09 Metallic Materials - Tensile Testing - Part 2: Method of Test at Elevated Temperture, Deutsches Institut für Normung e. V., Beuth Verlag, Berlin, 2018.
[42] DIN 50125, 2016-12 Testing of Metallic Materials - Tensile Test Pieces, Deutsches Institut für Normung e. V., Beuth Verlag, Berlin, 2016.
[43] German version EN ISO 204:2018, Metallic Materials - Uniaxial Creep Testing in Tension - Method of Test (ISO 204:2018), International Organization for Standardization, 2019.

[44] German version EN ISO 7500-2:2006, Metallic Materials - Verification of Static Uniaxial Testing Machines - Part 2: Tension Creep Testing Machines - Verification of the Applied Force (ISO 7500-2:2006), International Organization for Standardization, 2007, 4.
[45] E. e.V., Guidelines on the Calibration of Thermocouples, EURAMET Calibration Guide No. 8, Braunschweig, Germany, 2020.
[46] E. e.V., Guidelines on the Calibration of Temperature Indicators and Simulators by Electrical Simulation and Measurement, EURAMET Calibration Guide No. 11, Braunschweig, Germany, 2007.
[48] ASTM E112-13 Standard Test Methods for Determining Average Grain Size, ASTM International, West Conshohocken, PA, 2013.
[49] B. Skrotzki, J. Olbricht, H.-J. Kühn, High temperature mechanical testing of metals, in: S. Schmauder, C.-S. Chen, K.K. Chawla, N. Chawla, W. Chen, Y. Kagawa (Eds.), Handbook of Mechanics of Materials, Springer Singapore, Singapore, 2018, pp. 1–38.
[50] R. Casati, J. Lemke, M. Vedani, Microstructure and fracture behavior of 316L austenitic stainless steel produced by selective laser melting, J. Mater. Sci. Technol. 32 (8) (2016) 738–744, https://doi.org/10.1016/j.jmst.2016.06.016.
[51] P. Bajaj, A. Hariharan, A. Kini, P. Kürnsteiner, D. Raabe, E.A. Jägle, Steels in additive manufacturing: a review of their microstructure and properties, Mater. Sci. Eng., A 772 (2020) 138633, https://doi.org/10.1016/j.msea.2019.138633.
[52] S. Dryepondt, P. Nandwana, P. Fernandez-Zelaia, F. List, Microstructure and high temperature tensile properties of 316L fabricated by laser powder-bed fusion, Additive Manufacturing 37 (2021) 101723, https://doi.org/10.1016/j.addma.2020.101723.
[53] H. Ledbetter, Dynamic vs. static Young's moduli: a case study, Mater. Sci. Eng., A 165 (1) (1993) L9–L10, https://doi.org/10.1016/0921-5093(93)90634-Q.
[54] Z. Xu, C.J. Hyde, C. Tuck, A.T. Clare, Creep behaviour of inconel 718 processed by laser powder bed fusion, J. Mater. Process. Technol. 256 (2018) 13–24, https://doi.org/10.1016/j.jmatprotec.2018.01.040.
[55] T. Voisin, J.-B. Forien, A. Perron, S. Aubry, N. Bertin, A. Samanta, A. Baker, Y. M. Wang, New insights on cellular structures strengthening mechanisms and thermal stability of an austenitic stainless steel fabricated by laser powder-bed-fusion, Acta Mater. 203 (2021) 116476, https://doi.org/10.1016/j.actamat.2020.11.018.
[56] M. Sprengel, A. Ulbricht, A. Evans, A. Kromm, K. Sommer, T. Werner, J. Kelleher, G. Bruno, T. Kannengiesser, Towards the optimization of post-laser powder bed fusion stress-relieve treatments of stainless steel 316L, Metall. Mater. Trans. (in press), https://doi.org/10.1007/s11661-021-06472-6.
[57] K. Akino, K. Kakehi, Strengths and microstructure of SUS316L fabricated by selective laser melting, Journal of the Japan Institute of Metals and Materials 80 (12) (2016) 772–777, https://doi.org/10.2320/jinstmet.JAW201610.
[58] R.J. Williams, F. Vecchiato, J. Kelleher, M.R. Wenman, P.A. Hooper, C.M. Davies, Effects of heat treatment on residual stresses in the laser powder bed fusion of 316L stainless steel: finite element predictions and neutron diffraction measurements, J. Manuf. Process. 57 (2020) 641–653, https://doi.org/10.1016/j.jmapro.2020.07.023.
[59] P. Krakhmalev, G. Fredriksson, K. Svensson, I. Yadroitsev, I. Yadroitsava, M. Thuvander, R. Peng, Microstructure, solidification texture, and thermal stability of 316 L stainless steel manufactured by laser powder bed fusion, Metals 8 (8) (2018) 643.
[60] Q. Chao, S. Thomas, N. Birbilis, P. Cizek, P.D. Hodgson, D. Fabijanic, The effect of post-processing heat treatment on the microstructure, residual stress and mechanical properties of selective laser melted 316L stainless steel, Mater. Sci. Eng., A 821 (2021) 141611, https://doi.org/10.1016/j.msea.2021.141611.
[61] M.L.M. Sistiaga, S. Nardone, C. Hautfenne, J.V. Humbeeck, Effect of heat treatment of 316l stainless steel produced by selective laser melting (SLM), in: 2016 Annual International Solid Freeform Fabrication Symposium – an Additive Manufacturing Conference, University of Texas at Austin, Austin, Texas, USA, 2016.
[62] T. Ronneberg, C.M. Davies, P.A. Hooper, Revealing relationships between porosity, microstructure and mechanical properties of laser powder bed fusion 316L stainless steel through heat treatment, Mater. Des. 189 (2020) 108481, https://doi.org/10.1016/j.matdes.2020.108481.
[63] S. Takeuchi, A.S. Argon, Steady-state creep of single-phase crystalline matter at high temperature, J. Mater. Sci. 11 (8) (1976) 1542–1566, https://doi.org/10.1007/BF00540888.
[64] D. Morris, D. Harries, Creep and rupture in Type 316 stainless steel at temperatures between 525 and 900 C Part I: creep rate, Met. Sci. 12 (11) (1978) 525–531.
[65] J.K.L. Lai, A review of precipitation behaviour in AISI type 316 stainless steel, Mater. Sci. Eng. 61 (2) (1983) 101–109, https://doi.org/10.1016/0025-5416(83)90191-X.
[66] R. Stoltz, J. Vander Sande, The effect of nitrogen on stacking fault energy of Fe-Ni-Cr-Mn steels, Metallurgical Transactions A 11 (6) (1980) 1033–1037.
[67] O.D. Sherby, P.M. Burke, Mechanical behavior of crystalline solids at elevated temperature, Prog. Mater. Sci. 13 (1968) 323–390, https://doi.org/10.1016/0079-6425(68)90024-8.
[68] J.-P. Poirier, Creep of Crystals: High-Temperature Deformation Processes in Metals, Ceramics and Minerals, Cambridge University Press, Cambridge, 1985.
[69] R.E. Schramm, R.P. Reed, Stacking fault energies of seven commercial austenitic stainless steels, Metallurgical Transactions A 6 (7) (1975) 1345, https://doi.org/10.1007/BF02641927.
[70] H. Riedel, Fracture at High Temperatures, Springer Berlin Heidelberg1987.
[71] R.E. Smallman, A.H.W. Ngan, Chapter 15 - creep, fatigue and fracture, in: R. E. Smallman, A.H.W. Ngan (Eds.), Modern Physical Metallurgy (Eighth Edition), Butterworth-Heinemann, Oxford, 2014, pp. 571–616.
[72] M.F. Ashby, C. Gandhi, D.M.R. Taplin, Overview No. 3 Fracture-mechanism maps and their construction for f.c.c. metals and alloys, Acta Metall. 27 (5) (1979) 699–729, https://doi.org/10.1016/0001-6160(79)90105-6.
[73] T.M. Devine, The mechanism of sensitization of austenitic stainless steel, Corrosion Sci. 30 (2) (1990) 135–151, https://doi.org/10.1016/0010-938X(90)90068-G.
[74] A.S. Argon, Intergranular cavitation in creeping alloys, Scripta Metall. 17 (1) (1983) 5–12, https://doi.org/10.1016/0036-9748(83)90061-3.
[75] B. Weiss, R. Stickler, Phase instabilities during high temperature exposure of 316 austenitic stainless steel, Metall. Mater. Trans. B 3 (4) (1972) 851–866, https://doi.org/10.1007/BF02647659.
[76] C. Gandhi, M.F. Ashby, Overview no. 5: fracture-mechanism maps for materials which cleave: F.C.C., B.C.C. and H.C.P. metals and ceramics, Acta Metall. 27 (10) (1979) 1565–1602, https://doi.org/10.1016/0001-6160(79)90042-7.
[77] D.G. Morris, D.R. Harries, Wedge crack nucleation in Type 316 stainless steel, J. Mater. Sci. 12 (8) (1977) 1587–1597, https://doi.org/10.1007/BF00542809.
[79] D. Kong, C. Dong, S. Wei, X. Ni, L. Zhang, R. Li, L. Wang, C. Man, X. Li, About metastable cellular structure in additively manufactured austenitic stainless steels, Additive Manufacturing 38 (2021) 101804, https://doi.org/10.1016/j.addma.2020.101804.
[80] G.E. Dieter, D.J. Bacon, D. Bacon, in: Mechanical Metallurgy - SI, Metric ed., McGraw-Hill, 1988.
[81] J. Weertman, Dislocation climb theory of steady-state creep, Transactions of the American Society of Metals 61 (1968) 681–694.
[82] X. Zhang, M.D. McMurtrey, L. Wang, R.C. O'Brien, C.-H. Shiau, Y. Wang, R. Scott, Y. Ren, C. Sun, Evolution of microstructure, residual stress, and tensile properties of additively manufactured stainless steel under heat treatments, JOM 72 (12) (2020) 4167–4177, https://doi.org/10.1007/s11837-020-04433-9.
[83] P. Deng, H. Yin, M. Song, D. Li, Y. Zheng, B.C. Prorok, X. Lou, On the thermal stability of dislocation cellular structures in additively manufactured austenitic stainless steels: roles of heavy element segregation and stacking fault energy, JOM 72 (12) (2020) 4232–4243, https://doi.org/10.1007/s11837-020-04427-7.
[84] M.R. Stoudt, E.A. Lass, D.S. Ng, M.E. Williams, F. Zhang, C.E. Campbell, G. Lindwall, L.E. Levine, The influence of annealing temperature and time on the formation of δ-phase in additively-manufactured inconel 625, Metall. Mater. Trans. 49 (7) (2018) 3028–3037, https://doi.org/10.1007/s11661-018-4643-y.
[85] L.M. Suave, J. Cormier, P. Villechaise, A. Soula, Z. Hervier, D. Bertheau, J. Laigo, Microstructural evolutions during thermal aging of alloy 625: impact of temperature and forming process, Metall. Mater. Trans. 45 (7) (2014) 2963–2982, https://doi.org/10.1007/s11661-014-2256-7.
[86] S. Gao, Z. Hu, M. Duchamp, P.S.S.R. Krishnan, S. Tekumalla, X. Song, M. Seita, Recrystallization-based grain boundary engineering of 316L stainless steel produced via selective laser melting, Acta Mater. 200 (2020) 366–377, https://doi.org/10.1016/j.actamat.2020.09.015.